Applied Ocean Research 161 (2025) 104626

Contents lists available at ScienceDirect

Applied Ocean Research

journal homepage: www.elsevier.com/locate/apor

Research paper

Effects of wave spectrum representation on power production estimations from point absorbers

Matías Alday *, Vaibhav Raghavan, George Lavidas

Marine Renewable Energies Lab., Offshore Engineering group, Department of Hydraulic Engineering, Delft University of Technology, Stevinweg 1, Delft 2628 CN, The Netherlands

ARTICLE INFO

Dataset link: https://www.tudelft.nl/en/ceg/about-faculty/departments/hydraulic-engineering/sections/offshore-engineering/research/marine-renewable-energies-lab-mrel/datasets-models

Keywords:
Wave energy converters
Multi-modal spectrum
JONSWAP
HAMS-MREL

ABSTRACT

This study presents a first long term (30 years) assessment to quantify the effects of both, the wave spectrum representation, and occurrences of multi-modal sea states, on power production estimations from a point-absorber Wave Energy Converter (WEC). Analysis in 3 different offshore locations (Portugal, Ireland and The Netherlands) is included to ensure robustness of results. In general, traditional methods based on the use of the JONSWAP spectrum, with an adequate gamma shape value, can lead to mean overestimation in yearly power production > 12% when compared to reference hindcast spectral data. This can be partially reduced when capping is applied to power production, but still can be close to 10%. An alternative method is proposed to modulate the JONSWAP spectrum at each time step which helps to reduce differences, but leads to slight yearly underestimations (−2.5 to −5% in average). Although in all analyzed sites the occurrences of multi-modal spectra is > 30%, contribution to errors due to misrepresentation of these sea states are estimated to be of about 2.5%. These findings provide valuable insights on the uncertainties introduced in power production estimations, related to wave conditions characterization, that can have important economic impact when planning for large scale deployments.

1. Introduction

The accurate representation of sea states is the first key element to reduce the uncertainties in wave resource assessments. It is the quantification of the available resource that allows to define which sites are of interest for harvesting the energy from the waves (e.g; Guillou et al., 2020; Besio et al., 2016). With the areas of interest identified, the next logic step is to estimate the power production levels related to the wave energy converter (WEC) that is most suitable for the local sea states' conditions (Lavidas, 2020; Guillou and Chapalain, 2018; Kamranzad et al., 2017; Babarit, 2015). In fact, it is understood that the characteristics of a WEC farm, when planning for large scale deployments, should be defined based on a proper joint WEC–Site production analysis (Carballo et al., 2014). In order to accomplish the latter, the accuracy of the sea states information plays once again a primary role.

Before deployment or prototype construction, WEC power production estimations are typically done first through experimental (scaled) testing under controlled conditions (Rhinefrank et al., 2015; Kracht et al., 2015), and/or approximated using numerical models working on the spectral or time domain (Everett et al., 2024; Giassi et al., 2020). Regardless of the test approach (experimental or modeling) or the implemented WEC control type used to optimize energy yield, the device's response will be different depending on how the wave field is represented. For example, let us characterize the input for a wave palette or a WEC numerical model with the significant wave height (H_s) and the peak period (T_p). If these wave parameters are used to generate regular waves, modulate a JONSWAP (Hasselmann et al., 1973) spectrum, or correspond to a measured spectrum, the resulting wave field will be clearly different. When it comes to estimations of the production potential in specific sites, these different ways to represent wave conditions can introduce non-negligible discrepancies. Quantifying the effects of the wave spectrum representation on power production estimations, is the main concern of the present study.

The JONSWAP frequency spectrum is commonly employed in wave energy applications. Its use ranges from wave palettes control to generate random wave conditions in test tanks or flumes, to the spectral input

* Corresponding author.
E-mail addresses: M.F.AldayGonzalez@tudelft.nl, matias.alday@gmail.com (M. Alday), v.raghavan@tudelft.nl (V. Raghavan), g.lavidas@tudelft.nl (G. Lavidas).
URLs: https://www.researchgate.net/profile/Matias-Alday (M. Alday), https://www.researchgate.net/profile/Vaibhav-Raghavan (V. Raghavan), https://www.researchgate.net/profile/George-Lavidas (G. Lavidas).

https://doi.org/10.1016/j.apor.2025.104626
Received 19 November 2024; Received in revised form 30 April 2025; Accepted 20 May 2025
Available online 2 July 2025

in numerical models to simulate WEC responses. On the other hand, in the last 10 years or so, there have been significant improvements in spectral wave models like WAM (WAMDI Group, 1988), WAVEWATCH III (from hereon WW3; The WAVEWATCH III® Development Group, 2019) or SWAN (Booij et al., 1996). These have allowed the scientific and engineering community to better represent and understand wind-waves' dynamics from open ocean to coastal areas (e.g.; Ardhuin et al., 2010; Rascle and Ardhuin, 2013; Roland and Ardhuin, 2014; Alday et al., 2021, 2022). Nevertheless, the use of spectral time series from wave models is still not widely implemented in energy applications. This is specially the case of power production estimations, where simplified power matrices are employed to "summarize" WEC responses as a function of sea states' occurrences, characterized by H_s and T_p (or the energy period T_e).

One of the main advantages of modeled data, is its capability of reproducing a wide range of spectral shapes obtained with the combined effects of forcing fields and the implemented physical parameterizations. Additionally, models provide large time and spatial coverage. In contrast, commonly use parametric spectral shapes like JONSWAP, not only can introduce large errors in wave energy distributions in the absence of adequate shape parameters, but fail to represent more complex multi-modal sea states related to the simultaneous occurrence of different wave systems. In fact, several publications have shown that the occurrence of more than one wave system (in open waters or coastal areas) is more of a general rule than an exception (e.g.; Vettor and Soares, 2020; De Leo et al., 2024; Portilla-Yandún, 2018; Langodan et al., 2015; Semedo et al., 2011). With this in mind, the following question arises: How much does the spectral representation of sea states and multi-modality affect power production estimations? Certainly pervious efforts have been made to quantify differences in WEC's absorbed/produced power related to spectral shapes. Nevertheless, these studies contemplate short time windows and/or only one specific location, or idealized conditions (e.g.; Prendergast et al., 2018; Maisondieu and Boulluec, 2016; Clabby et al., 2012).

In this study, we present a first long term (30 years) analysis on the effects of the spectral shapes and multi-modality over wave power production estimations. The proposed methodology includes the characterization of wave conditions in terms of occurrences of multi-modal sea states. This is done to provide an idea about the suitability of using parametric spectral shapes at a given location. Then, to estimate power production levels, numerical simulations of a point absorber WEC are carried out using the boundary element model HAMS-MREL (Raghavan et al., 2024). Three different approaches to define the spectral input of the WEC model are considered: (i) spectra time series generated using the JONSWAP formulation proposed by Goda (1999) with a fixed shape parameter, (ii) using the original JONSWAP expression by Hasselmann with variable shape parameters per time step, and (iii) using a time series of modeled spectra taken from the hindcast developed by Alday and Lavidas (2024). With these spectral input types, differences in the power production are estimated for the 30 years period at 3 locations with different wave climates, off the coasts of Portugal, Ireland, and The Netherlands. The use of these 3 selected locations, with different mean wave climates, helps to provide more clarity regarding the expected range of differences in produced power estimations. The proposed analysis aims to improve our understanding of the inaccuracies introduced when simplified spectral shapes are used in production assessments.

In the present paper, generalities about the directional and multi-modal spectra are presented in Section 2. WEC model employed, analysis proposed and used database are detailed in Section 3. Then results and discussions are included in Section 4, with conclusions following in Section 5.

2. About the directional and multi-modal spectra

The wave directional spectrum provides information about the distribution of wave energy (or density) in 2 dimensions (Donelan et al., 1985; Phillips, 1985; Hasselmann et al., 1980, 1973). It can be defined in the wave number space $E(k_x, k_y)$ or $E(k, \theta)$, where k is the magnitude of wave number vector and θ the wave direction, or as typically done, in terms of frequencies and direction $E(f, \theta)$. The directional spectrum obtained from state of the art spectral models, like WW3, TOMAWAK (Benoit et al., 1997) or SWAN, in situ measurements (Strong et al., 2000; Young, 1994), or some remote sensing techniques (e.g.; Hauser et al., 2020; Kudryavtsev et al., 2017; Wyatt et al., 2011; Hwang et al., 2000), allows to identify many characteristics from the sea states outside the commonly used parameters to describe wave conditions: H_s (significant wave height), D_m (mean direction) and T_p (peak period). Although their use is widely accepted in many engineering applications, they tend to oversimplify the description of the wave fields which, in many cases, can introduce errors or larger uncertainties in the corresponding analyses. In recent years, many studies have been carried out highlighting the necessity of using more detailed spectral information in different practical applications, and proposing different methods to facilitate interpretation of the data (e.g.; De Leo et al., 2024; Portilla-Yandún et al., 2019; Hegermiller et al., 2017; Bradbury et al., 2007).

When using directional spectral information, it is easy to observe the occurrence of co-existing "wave systems" which could correspond to one or more swells that have traveled long distances, together with locally generated waves or wind–seas (e.g. Fig. 1.b). A common approach to identify and characterize the different wave systems present in the directional spectrum, is through partitions. A spectral partition can be thought of as a subset of frequencies and directions that define the spectral region which corresponds to an independent wave system. Thus, once these partitions are identified, it is possible to characterize each wave system with its own set of parameters obtained from integration of the corresponding spectral region (Hanson and Phillips, 2001; Hasselmann et al., 1996; Gerling, 1992). For example, in Fig. 1 it is easy to define, only by observation, 2 and 3 main partitions in Fig. 1.a and Fig. 1.b respectively (left panels). In real applications, where large datasets are analyzed, wave partitioning requires specific algorithms. There are several proposed methods to perform spectral partitioning which can be roughly divided in 3 main groups: Based on wave age with frequency level cutoff to identify wind–seas and swells (e.g.; Tracy et al., 2007; Hanson and Phillips, 2001), based on applications of watershed algorithms (e.g.; Hanson and Jensen, 2004; Hasselmann et al., 1996; Gerling, 1992; Vincent and Soille, 1991) and, as proposed in Kpogo-Nuwoklo et al. (2014), a group based on parameter optimization methods (e.g.; Ailliot et al., 2013; Boukhanovsky and Guedes Soares, 2009).

Although spectral partitioning aims to provide more detailed information from the sea states in a comprehensive way, its use (or in general the directional wave spectrum) is relatively recent in wave energy applications, specially in produced power estimations from WECs (Ribeiro et al., 2020; Esmaeilzadeh and Alam, 2019; Kerbiriou et al., 2007). Instead, the "omnidirectional" or frequency spectrum is typically employed. The frequency spectrum can be obtained from integration of the directional spectrum (see Eq. (1)) or directly from measurements (like pressure sensors or buoys).

$$E(f) = \int_0^{2\pi} E(f, \theta)\, d\theta \tag{1}$$

Generally, the term multi-modal is used for omnidirectional spectra with more than one peak of energy within the considered range of frequencies. These peaks of energy are indeed related to the wave systems from a given sea state. Taking the example presented in Fig. 1 it is possible to observe that, by integrating the directional spectrum, wave systems' information (described by partitions) can be significantly lost. In Fig. 1.a, where the directional spectrum presents 2 swell systems, the most energetic coming from the North (A), and the secondary (B) arriving from the SW (243°), the obtained frequency spectrum shows what is usually called an uni-modal spectrum. Basically, a frequency

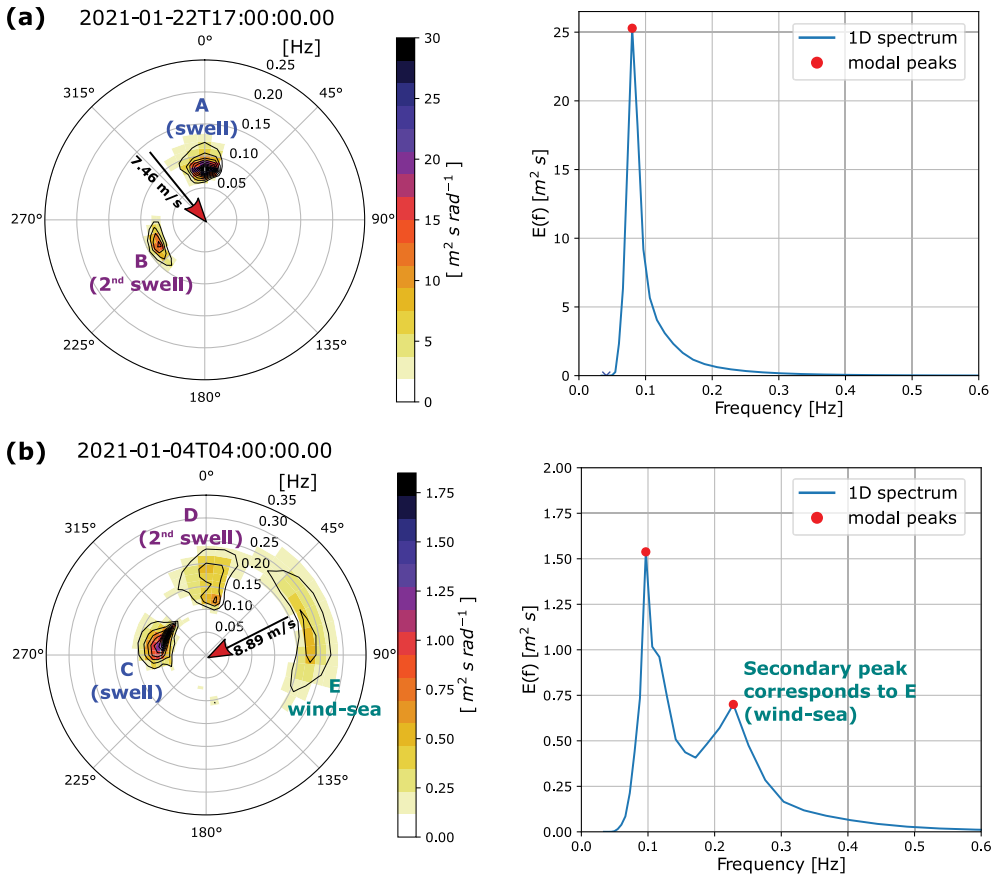

Fig. 1. Examples of uni-modal and bi-modal spectra obtained from integration of directional spectrum with (a) 2 swell systems, and (b) 2 swell systems and one developing wind–sea. Arrows indicate the local wind direction. For wind and wave, convention is "direction from". Wave spectra obtained from the ECHOWAVE hindcast at longitude −10.9°, latitude 52.85°.

spectrum with a single energy (or density) peak. This happens when each wave system has its local peak in similar frequencies. In this case 0.08 and 0.82 Hz for swell A and B respectively (or $T_{p,A}$ = 12.47 s and $T_{p,B}$ = 12.13 s). In Fig. 1.b a similar situation is observed with 3 wave systems identified in the directional spectrum. The most energetic swell C comes from the WNW (295°) with $T_{p,C}$ = 10.42 s, a secondary "younger" swell D arriving from the *N* (8.5°) with $T_{p,D}$ = 8.33 s, and from the ENE (80.8°) a developing wind–sea E with $T_{p,E}$ = 4.50 s. Note how the wind–sea is closely aligned with the local wind (Fig. 1.b, left panel). In this case the computed frequency spectrum is bi-modal (two energy peaks), where the secondary peak is obtained mainly due to the contribution of the wind–sea.

It is clear that, in general, the loss of the directional component in spectral information can lead not only to inaccuracies in the sea states characterization, but also in WECs' design and performance estimations (Esmaeilzadeh and Alam, 2019; Adibzade and Akbari, 2024). This is specially true when the converters' power capture is sensitive to incoming waves' direction, as it is for the "flap type" WECs (Henry et al., 2018). Nevertheless, for point absorber type devices, where heave motion is dominant, effects of wave directionality are negligible when analyzing the performance of a single WEC. In this case, the accuracy of the frequency spectrum becomes the first key condition to reduce uncertainties in power production estimations.

3. Materials and method

3.1. Wave dataset

Wave spectral data is taken from the ECHOWAVE hindcast developed at the Marine Renewable Energies Lab (MREL). This 30 years high-resolution dataset was created using WW3 implemented with a regular multi-grid 2-way nesting system (Tolman, 2008; Chawla et al., 2013), and adjustments specially aimed to improve its accuracy in Atlantic European coastal waters, which lead to the TUD-165 set of parameterizations. The wave spectrum is discretized in 36 directions and 36 exponentially spaced frequencies from 0.034 to 0.95 Hz, using a 1.1 increment factor from one frequency to the next. The maximum spatial resolution within the European coastal shelf is ~2.3 km. To force the model, the following fields were considered:

- ERA5 winds (Hersbach et al., 2020) for wave generation.
- COPERNICUS-GLOBCURRENT surface global (quasi-geostrophic) currents (CMEMS product MULTIOBS_GLO_PHY_REP_015_004).
- The ice concentration from Ifremer SSMI-derived product (Girard-Ardhuin and Ezraty, 2012) considering a 1 m constant thickness.
- Tidal levels and currents taken from the Atlantic-European North West Shelf-Ocean Physics Reanalysis (CMEMS product NWSHELF_MULTIYEAR_PHY_004_009).

For further details on the hindcast's parameterization adjustments and validation, please refer to Alday and Lavidas (2024).

3.2. Identification of multi-modal sea states

The occurrences of single peaked, bi-modal, tri-modal, or spectra with ≥4 peaks is used to characterize the local wave conditions at 3 sites: Viana do Castello in Portugal (POR), western Ireland (IRE), and off the coasts of The Netherlands (NED). Detailed location and depths information from these sites is presented in Fig. 2.

A slightly modified version of the peaks identification method from Rodrıguez and Guedes Soares (1999) (from hereon RGS-99) was used as

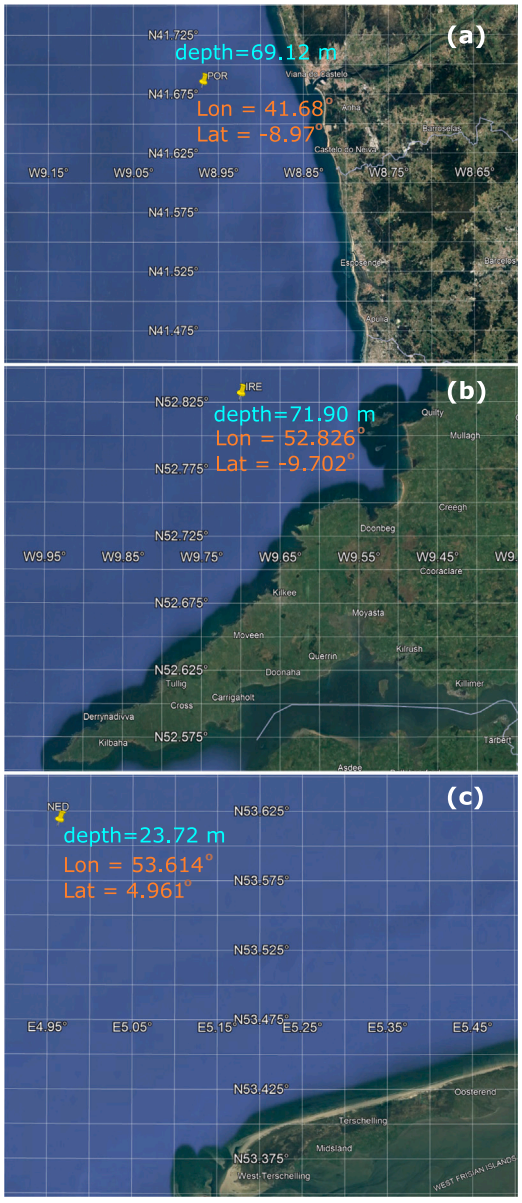

Fig. 2. Locations and depths of sites where spectral multi-modality is analyzed. (a) POR, (b) IRE, and (c) NED. Mean depths (with respect to mean sea level) are obtained from the ECHOWAVE hindcast spectral files.

the main multi-modality characterization approach. This method was adopted due to the simplicity of its implementation, and because the present study is focused on the occurrences of multi-modal spectra, instead of the physical nature of the identified peaks. With RGS-99, the identification of the spectral peaks is done over a logarithmic-scaled frequency spectrum $\ln(E(f))$. Then, to accept an identified peak as such, the imposed criterion is that the "amplitude" of the peak (measured from the previous minimum) must be higher than the estimated width of a confidence interval (Eq. (2)) related to the "spectral estimates" in logarithmic scale.

$$\text{Conf.interval} = \ln\left(\frac{\nu}{\chi^2_{\nu,1-\alpha/2}}\right) - \ln\left(\frac{\nu}{\chi^2_{\nu,\alpha/2}}\right) = \ln\left(\frac{\chi^2_{\nu,\alpha/2}}{\chi^2_{\nu,1-\alpha/2}}\right) \quad (2)$$

The confidence interval defined in Eq. (2) represents the 90% probability that true value of $\ln(E(f))$ is placed between the following limits:

$$\left[\ln(E(f)) - \ln\left(\frac{\nu}{\chi^2_{\nu,\alpha/2}}\right), \ln(E(f)) + \ln\left(\frac{\nu}{\chi^2_{\nu,1-\alpha/2}}\right)\right] \quad (3)$$

In Eqs. (2) and (3), α is the confidence level (here set to 0.1), with $\chi^2_{\nu,\alpha/2}$ and $\chi^2_{\nu,1-\alpha/2}$ the $100(\alpha/2)^{th}$ and $100(1-\alpha/2)^{th}$ percentiles from a chi-squared random variable considering ν degrees of freedom. Note that for the RGS-99 approach, using a logarithmic-scaled spectrum, with fixed values of α and ν, the confidence interval width becomes a single value that can be used for all frequencies.

Rodrıguez and Guedes Soares (1999) analyzed the smoothness effects related to the different degrees of freedom ν used to estimate the frequencies spectrum from synthetic sea surface elevation series. Based on their analysis, they recommend using $\nu = \sim 40$ to ensure obtaining the "true" number of peaks. Since in this study modeled spectral data is used, which can be considered as "smooth", a value of $\nu = 50$ is employed for all calculations.

Here, an extra step is included to the original RGS-99 method. A minimum spectral energy level threshold is applied. After the identification of the local maxima in the scaled spectrum $\ln(E(f))$, the energy level of the peaks, in the original spectrum $E(f)$, is compared to this threshold. If the energy at the local peak is larger than the set threshold, then the peak is kept. Additionally, if no peak is kept due to the imposed minimum threshold, the sea state is considered uni-modal. This modification was introduced to avoid considering unnecessary peaks in very low energetic sea states from the modeled spectra, which might be subjected to numerical inaccuracies. To evaluate the effects of the minimum energy threshold in the multi-modal occurrences, a sensitivity analysis with values of 0.0, 0.02 and 0.05 m^2 s is performed.

Other approaches may be considered to perform multi-modality characterization. For example, in the method proposed by Wang and Hwang (2001), the separation of wind–sea and swell components of the omnidirectional spectrum is done from a physical point of view, considering frequency depending wave steepness. Nevertheless, in the present study the complexity of the energy distribution in the spectrum is the main focus, which makes RGS-99 a proper tool for spectra characterization.

3.3. Wave energy converter response modeling

The end goal of the WEC's response simulation is to estimate the power absorbed by the device. The hydrodynamic modeling for the WEC is done in the frequency domain with a weakly non-linear formulation. The model considers input from a time series of omnidirectional spectra to account for irregular sea states. For each time step of 1 h, a variance spectrum and its related wave parameters H_s, T_p and the energy period T_e are used as input. This approach deviates from the traditional use of power matrices, where the response of the WEC for a given sea state characterized by (H_s, T_p) would remain constant, even if the spectral energy distribution is different. It is important to highlight that, with the proposed method here, the response of the device can vary as a function of the input spectrum, or the spectral description of the sea state conditions (which is the main subject of this study). Basically, the excitation force is related to the spectral description of the incoming sea states. Then, adjustments of the Power Take-Off (PTO) are optimized for a given sea state (per time step). Thus, the dynamic response of the WEC changes, and as a consequence of the changes in the dynamic response, there is a change in the production estimation.

The wave energy converter considered is a point absorber, its geometry and mass properties are inspired by the Corpower C4 device (Corpower, 2023). The dimensions of the device are given in Table 1. The draft of 6 m was assumed by the authors for this study and the natural frequency was calculated based on the aforementioned properties. A weakly non-linear frequency domain model, only

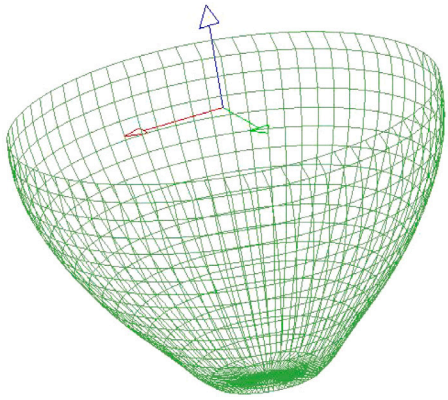

Fig. 3. Mesh of point absorber modeled using HAMS-MREL.

Table 1
Properties of the Corpower C4 device.

Property	Value	Unit
Diameter	9	m
Height	18	m
Installation depth (minimum)	40	m
Weight	70	tonne
Buoy draft	6	m
Undamped natural period (heave)	3	s

considering heave motion, was used in estimating the motion of the device per frequency, considering viscous losses. The viscous losses are calculated using the spectral domain method (Tan et al., 2023; Folley and Whittaker, 2010, 2013; Silva et al., 2020), which are well suited for irregular sea states.

The PTO control of the device is incorporated employing the following considerations for optimal passive control: (i) Canceling the PTO reactance (also referred to as the stiffness coefficient for the PTO system) which essentially occurs at resonance, and (ii) The PTO damping should be equal to the impedance which ensures maximum power absorption. For most practical cases, the PTO reactance is negligible or zero and so considering just the PTO damping condition is sufficient (Alves, 2016). This has been incorporated based on the work of Hals et al. (2002), taking into account the viscous losses without any constraints.

To estimate the viscous losses in the spectral domain, the standard deviation of the heave velocity of the WEC across all frequencies is required. Since the passive PTO damping and viscous losses are interdependent, an iterative process is employed to obtain the optimized values of these parameters (further details given below).

The motion for the ith frequency ω_i is estimated with the following expression:

$$[-\omega_i^2(m_d + m_{a,i}(\omega_i)) + i\omega_i(b_{a,i}(\omega_i) + b_{PTO} + b_v) + c_h]s = f_{e,i}(\omega_i) \tag{4}$$

where the first 2 terms are the mass of the device m_d and the added mass heave hydrodynamic coefficient $m_{a,i}$. Then, $b_{a,i}$ is the radiation damping heave hydrodynamic coefficient, b_{PTO} is the PTO coefficient for the device, b_v is the linearized viscous damping coefficient. Finally, c_h is the hydro-static stiffness heave coefficient, $f_{e,i}$ is the heave exciting force, and s is the displacement amplitude of the device also referred to as the body excursion. When the amplitude of the incident wave is 1 m, then s represents the RAO (Response amplitude Operator) in heave motion for the device.

The frequency dependent hydrodynamic coefficients and exciting forces are obtained from the frequency domain Boundary Element Method (BEM) solver HAMS-MREL (Raghavan et al., 2024). The mesh employed for running the simulations in HAMS-MREL is shown in Fig. 3. A representative depth of 70 m is considered for POR and IRE, and 23 m for NED. Optimal passive control including viscous losses was incorporated. The optimum PTO damping coefficient for any given frequency can be derived using (5), assuming no constraint.

$$b_{PTO}(\omega) = (R(\omega)^2 + X(\omega)^2)^{1/2} \tag{5}$$

where

$$R(\omega) = b_a(\omega) + b_v \tag{6}$$

and

$$X(\omega) = i\omega[m_d + m_a(\omega)] + (c_h/i\omega) \tag{7}$$

where $R(\omega)$ and $X(\omega)$ are the real and imaginary parts of the intrinsic impedance of the heaving body. In order to estimate the optimal passive PTO coefficient for a given irregular sea state, the energy period T_e is utilized, since it is based on the average energy distribution across all frequencies in the spectrum (Mazzaretto et al., 2022). The hydrodynamic coefficients and exciting forces in heave, are estimated for this regular sea state and then used to estimate the optimal passive damping coefficient b_{PTO} to be used for all frequencies. The energy period is estimated from the spectra (De La Torre et al., 2023) as:

$$T_e = \frac{m_{-1}}{m_0} \tag{8}$$

where m_{-1} and m_0 are the spectral moments of the order −1 and 0 respectively.

The following steps were considered to estimate the response of the WEC (per time step):

- To start the process of estimating the response, first the PTO coefficient b_{PTO} and viscous damping coefficient b_v are estimated. The initial estimate of b_v is derived from Lorentz' linearization (based on McNatt and Retzler, 2020). This is calculated as follows:

  $$b_v = \frac{4}{3\pi} C_D \rho A_D \tag{9}$$

  where ρ is the density of water, C_D is the viscous drag coefficient (taken to be 0.25 based on the work of Shao et al., 2024) and A_D is the characteristic area of the WEC.
  This obtained b_v is used to calculate the initial estimate of the optimal PTO coefficient b_{PTO} using Eq. (5). The equation of motion for all considered frequencies is then solved with Eq. (4) using b_{PTO} and b_v.
- For the second iteration, the damping coefficient b_v is estimated using the spectral domain method, given by:

  $$b_v = \frac{1}{2}\rho C_D A_D \sigma_u \sqrt{\frac{8}{\pi}} \tag{10}$$

  σ_u is the standard deviation of the velocity across all considered frequencies. This is followed by the next estimation of the b_{PTO} and thus the computation of the response using the equations of motion. This procedure is repeated until the Mean Squared Error (MSE; see Eq. (11)), between the predicted responses from two consecutive steps is within a tolerance of $1e^{-6}$.

  $$MSE = \frac{1}{N}\Sigma(S_n - S_p)^2 \tag{11}$$

  In Eq. (11), S_n is the new vector of responses (latest step) and S_p is the previous estimation of responses (previous step) over all considered N frequencies. The value of N is taken as 36 based on the spectral discretization used in WW3 (ECHOWAVE).

For the computation of b_{pto}, lower tolerance levels were also considered as a sensitivity analysis test. This exercise showed negligible changes since the iteration process quickly reaches changes of the MSE close to $1e^{-8}$ after 2 iterations.

Once the responses per frequency for a given time step are estimated, the power is estimated (Penalba et al., 2017) with the variance spectra as:

$$P_{irr} = \int_0^\infty 2P(\omega)S(\omega)d\omega \tag{12}$$

where $P(\omega)$ is the power spectra over all considered frequencies with power for the ith frequency given as:

$$P_i = \frac{1}{2} b_{PTO}\omega_i^2 |s_i|^2 \tag{13}$$

and $S(\omega)$ is the variance spectra representing the time series of a given time step.

The power estimations with the above procedure provides the unconstrained power produced by the heaving device (as used in Section 4.3). Three additional cases are also shown, where the maximum allowed power from the device, at any given time step, is restricted to 300, 400 and 500 kW (capping) respectively. These are considered since, for large wave heights (e.g.; >6 m), the forces developed in the PTO can be quite large, and as a consequence, also the estimated power will be high. The "capped power" case is also considered to demonstrate the influence of wave resource (high or low) on the capacity factor (see Section 4.4).

3.4. Spectral representation

The wave spectra, employed as input for the simulations of the WEC response, is prescribed using 3 different approaches. First, based on the time series of H_s and T_p of each analyzed location taken from the wave hindcast (Fig. 2), a JONSWAP spectra time series is created with a single gamma value (γ) using the simplified expression proposed in Goda (1999) which is written as a function of H_s and T_p:

$$E(f)_{\text{Goda}} = \beta_J {H_s}^2 {T_p}^{-4} f^{-5} \exp\left[-1.25(T_p f)^{-4}\right] \gamma^{\exp\left[-(T_p f-1)^2/(2\sigma^2)\right]} \tag{14}$$

where

$$\beta_J = \frac{0.0624}{0.230 + 0.0336\gamma - 0.185(1.9+\gamma)^{-1}} [1.094 - 0.01915\ln(\gamma)] \tag{15}$$

and

$$\sigma = \begin{cases} \sigma_a = 0.07\ , f \le f_p \\ \sigma_b = 0.09\ , f > f_p \end{cases} \tag{16}$$

The gamma value γ in Eqs. (14) and (15) ranges from 1 to 7 (Goda, 1999). This approach to define the spectral input is referred to as JON-G.

For JON-G cases, γ is computed as the average from the best fit found between each (hourly) wave spectrum from the ECHOWAVE hindcast and Eq. (14), considering only those γ values where the Pearson correlation index between the best fit obtained spectra and the modeled spectra is >0.95.

The second approach to define the input for WEC simulations, from hereon called JON-H, is slightly different. In this case the spectral input is defined using the original JONSWAP expression proposed by Hasselmann et al. (1973):

$$E(f)_{\text{Hasselmann}} = \alpha g^2 (2\pi)^{-4} f^{-5} \exp\left[-\frac{5}{4}\left(\frac{f}{f_p}\right)^{-4}\right] \gamma^{\exp\left[-\frac{1}{2}\left(\frac{f-f_p}{\sigma f_p}\right)^2\right]} \tag{17}$$

where σ is the same as given in Eq. (16).

Note that Eq. (17) is a function of 4 parameters (g = 9.81 ms^2 is the acceleration of gravity). α is the Phillips constant and f_p is the frequency of the spectral peak. Then, γ and σ are shape parameters. In general for Eqs. (14) and (17), γ is called the peak-enhancement factor which controls the sharpness of the spectral peak.

To create the hourly time series of spectra using JON-H, f_p is taken from the hindcast data, the discrete frequencies (f) to define the spectrum are the same as the ones considered in the spectral files from the wave dataset. With this, it is already possible to define the values taken by σ following Eq. (16). To define γ and α, a best fit algorithm based on parameter optimization was implemented in Python (Van Rossum and Drake, 2009; Pilgrim and Willison, 2009). Basically, an objective function is created, in this case the squared sum of the discrete values (for each frequency) between the spectrum from Eq. (17) and the modeled data from ECHOWAVE. Then, the squared differences are minimized through iterations using the minimize function from Python's SciPy package (Virtanen et al., 2020). The detailed implementation of the script is included in Appendix A with thoroughly placed comments to facilitate its use. The same script was employed to obtain γ for Eq. (14). Particularly for JON-H, other methods to select γ and α could be implemented, like the one proposed in Rueda-Bayona et al. (2020) based on generic algorithms.

Finally, the time series of frequency spectra as given by the wave hindcast is employed for the WEC simulations. This latter case is referred to as the "full spectral representation" (FSR) approach. Note that the proposed method is designed to progressively increase the wave spectral energy distribution details, across the range of frequencies, for the input of the wave energy converters' simulations. Thus, JON-G is similar to the most common (and simple) approach to use wave parameters and the JONSWAP spectrum in many engineering applications. With JON-H a more accurate estimation of the spectral energy with the original JONSWAP expression is provided, using adequate α and γ values to modulate the spectra per time step. And then, by using the FSR approach, occurrences of multi-modal sea states are effectively being considered in the estimations of produced power.

A practical example is presented in Fig. 4 to visualize changes in the sea surface elevation related to a specific sea state condition. Here, synthetic time series of sea surface elevations were created based on the spectrum obtained with JON-G, JON-H and directly from the hindcast. The same (normally distributed) random phases Θ_i were considered for each time series, amplitudes related to each frequency component $a(f_i)$ are obtained from the spectrum following Eq. (18). The synthetic time series are created using the expression in Eq. (19).

$$a(f_i) = \sqrt{2E(f_i)\Delta f_i} \tag{18}$$

$$\eta(t) = \sum_{i=1}^{n} a(f_i) cos\left(2\pi f_i t + \Theta_i\right) \tag{19}$$

In Eqs. (18) and (19), f_i are the discrete frequencies used in the wave spectrum. $\eta(t)$ in Eq. (19) is the time series of sea surface elevations.

3.5. Differences quantification

To quantify the changes in spectral energy distribution and produced power estimations, the Mean Differences (MD), Normalized Mean Differences (NMD) and Scatter Index (SI) are employed:

$$\text{MD}(X) = \frac{1}{N}\sum(X_a - X_b) \tag{20}$$

$$\text{NMD}(X) = \frac{\sum(X_a - X_b)}{\sum X_b} \tag{21}$$

$$\text{SI}(X) = \sqrt{\frac{\sum\left[(X_a - \overline{X_a}) - (X_b - \overline{X_b})\right]^2}{\sum X_b^2}} \tag{22}$$

In Eqs. (20)–(22) X_a and X_b can be the hourly time series of spectra obtained with JON-G, JON-H or FSR, or the estimated produced power obtained from WEC simulations (see Section 3.3) using different wave spectra input. For example X_a could be the obtained time series of produced power using JON-G and X_b the one obtained using FSR.

It should be noticed that many other skill parameters could be used to assess differences or accuracy of a dataset with respect to a reference. For example the Hanna Heinhold index, the Anomaly Correlation Coefficient or the Murphy Skill Score, in addition to the

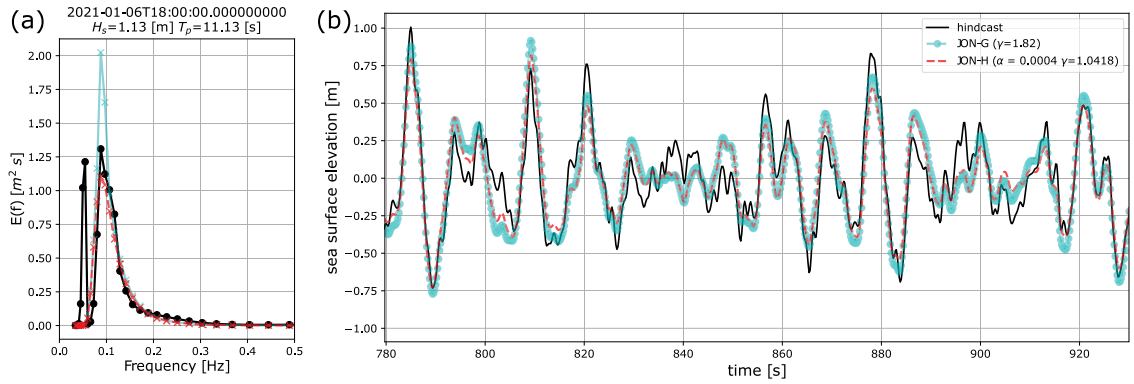

Fig. 4. Example of (a) spectral shapes obtained with JON-G, JON-H and FSR, and (b) synthetic time series of sea surface elevations created using spectrum from (a).

ones selected for this analysis, can be found in many publications (e.g.; Murphy, 1988; Murphy and Epstein, 1989; Mentaschi et al., 2015; Perignon, 2017; Alday et al., 2021; Beyramzadeh and Siadatmousavi, 2022).

4. Results and discussion

4.1. Sites' spectral characterization

As described in Section 3.2, characterization of the wave conditions at each analyzed location (POR, IRE and NED) is done in terms of the occurrences of single and multi-peaked frequency spectra. For robustness, the complete 30 years of spectral data from the wave hindcast is used. Results are presented in Table 2.

It was verified that slight changes in the levels of the minimum spectral energy threshold can significantly modify the total amount of multi-modal sea states occurrences. At POR, the total multi-modal occurrences (that is the sum of bi-modal, tri-modal and spectra with more than 4 spectral peaks) ranges from 48.4% to 38.72% when the minimum energy threshold goes from 0.0 to 0.05 m^2 s. Changes of the same order are found at IRE and NED where the total occurrences of multi-modal sea states go from 37.29% to 27.03%, and 51.88% to 38.76% respectively. Note that these reductions of about 10 % in the multi-modal occurrences are similar to the increase in uni-modal occurrences when the minimum spectral energy threshold varies from 0.0 to 0.05 m^2 s.

Regardless of the energy threshold used to characterize multi-modality at each location, it is clear that the occurrences of multi-modal sea states at each analyzed site are significant. Considering as representative the results using a threshold of 0.02 m^2 s, it is possible to observe that about 33%, 25% and 35% of the time the sea states are bi-modal at POR, IRE and NED respectively. Although not too frequent, tri-modal sea states have a non negligible level of occurrences of 7.9, 5.3 and 8.9% of the time at POR, IRE and NED. It should be noticed that NED is the location with the highest occurrences of multi-modal sea states. These results already suggest that the use of the JONSWAP spectrum will introduce differences (or errors) in the wave energy distribution in all 3 locations. Over 30% of the time the sea states will not be fully represented if JON-G or JON-H is employed.

The introduction of the energy threshold could be of interest when the peaks identification procedure is applied to spectral data obtained from measurements. For these cases, the threshold can be adapted to match the intrinsic noise level of the instrument where applying the original RGS-99 method might lead to spurious peaks detection during low energy sea states. It would probably be adequate to apply a frequencies dependent threshold, since it is expected to have different levels of accuracy (or noise) that are also a function of the frequencies range of a given instrument (e.g.; Liu et al., 2015; Ashton and Johanning, 2015).

Table 2
Estimated occurrences of uni-modal, bi-modal, tri-modal and spectra with more than 4 peaks using 30 year of modeled spectral data.

Location	min. E(f)	Modal occurrences [%]			
	threshold $m^2 s$	Uni-Modal	Bi-Modal	Tri-Modal	>4 spectral peaks
POR	0.0	51.603	36.582	9.442	2.372
	0.02	57.614	33.419	7.929	1.012
	0.05	61.247	31.301	6.737	0.678
IRE	0.0	62.703	29.144	6.445	1.707
	0.02	68.872	25.028	5.273	0.792
	0.05	72.925	22.377	4.154	0.498
NED	0.0	48.120	37.785	9.107	4.987
	0.02	53.639	35.201	8.967	1.933
	0.05	59.638	31.357	6.625	0.776

4.2. Spectral accuracy and validation of the best fit method to obtain JONSWAP parameters

To better understand potential changes in the power production estimations, it is of interest to first analyze the differences in the spectral energy distribution along the frequencies range. The assessment of the "spectral accuracy" is done following the approach proposed by Perignon (2017), estimating the mean, MD, NMD and SI of spectral energy at each discrete frequency. This assessment is done in 2 steps. First, the time series of spectra obtained with JON-G and JON-H are compared with ECHOWAVE's spectra using only sea states identified as uni-modal. This first step is used to validate the proposed best fit method to obtain the JONSWAP's α and γ parameters. The second step of the analysis is aimed to quantify the inaccuracies introduced when the frequency spectrum is estimated with JON-G or JON-H (which do not take into account multi-modality), compared to the reference spectra taken from the wave hindcast. In this case, the full time series is used to compute the performance parameters. Note that here, a γ value of 3.3 is adopted when using the JON-G approach to reconstruct the spectra time series. This value is employed as an example since it is commonly used in many application when no detailed spectral information is provided. Results for year 2021 at locations IRE and NED are presented in Figs. 5 and 6 respectively. Note that the frequencies presented, correspond to the range where changes of the performances parameters are more pronounced.

When analyzing the results at IRE, comparing only with uni-modal sea states (Fig. 5.a), it is possible to observe the clear overestimation of spectral energy in the neighborhood of 0.08 Hz when a fixed 3.3 gamma value is used with JON-G (MD = ~2.4 m^2 s, NMD = ~26%). These differences are of great importance since they occur in the frequencies range where most of the energy carried by waves is concentrated at this location. On the other hand, when JON-H is employed, the overestimation is effectively reduced with MD ranging between −0.33 and 0.35 m^2 s and NMD close to 0% between frequencies of 0.06 and

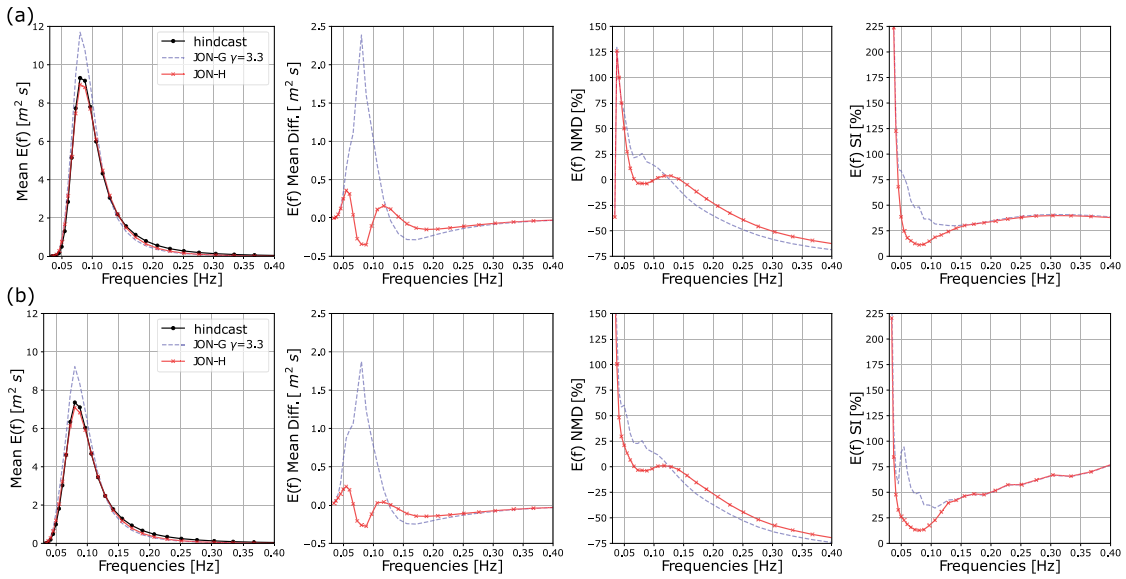

Fig. 5. Performance parameters of JON-G ($\gamma = 3.3$) and JON-H compared to ECHOWAVE spectral data using (a) uni-modal sea states only, and (b) full time series of spectra at IRE. Analyzed year: 2021.

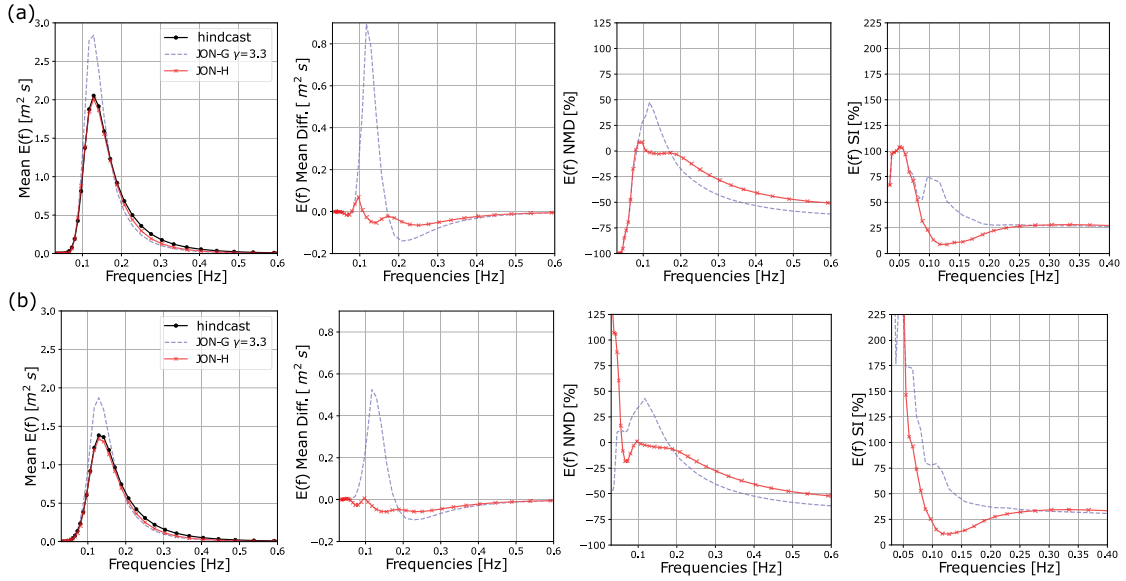

Fig. 6. Performance parameters of JON-G ($\gamma = 3.3$) and JON-H compared to ECHOWAVE spectral data using (a) uni-modal sea states only, and (b) full time series of spectra at NED. Analyzed year: 2021.

0.015 Hz. Although NMD values for frequencies <0.05 Hz are very high, these are related to low energy values (similar to what happens at frequencies >0.3 Hz). Particularly interesting is the reduction of the SI between 0.05 and 0.10 Hz when JON-H is employed, reaching a minimum value of 11% at 0.08 Hz. Note that both methods, JON-G and JON-H, present similar SI levels for frequencies >0.15 Hz when compared with the hindcast's spectral data.

In general, when comparing only uni-modal sea states, the largest NMD and SI values are obtained for frequencies <0.05 Hz and >0.15 Hz. This is true when comparing modeled spectra either with spectra generated with JON-G or JON-H. This is a direct consequence on the different representations of the wave energy distribution and its evolution in time. While the parametric one-dimensional JONSWAP spectrum is "modulated" based on f_p, α, γ and σ to incorporate wind speed and fetch dependence, the time evolution of the directional spectrum in the wave model is obtained with the integration (and balance) of the source terms which incorporate different parameterizations of physical processes.

The mean differences (MD) and NMD behavior at IRE, when comparing JON-G and JON-H with the full time series of spectra (Fig. 5.b), are similar to the results obtained using only uni-modal sea states (Fig. 5.a). In this case, most interesting changes are observed in the scatter index, with a clear increase of its values for frequencies >0.1 Hz, even doubling the SI levels at frequencies >0.15 Hz compared to Fig. 5.a (furthest right panel). This is a good example of the shortcomings of reconstructing spectrum without including its multi-modality. Note that the SI levels in the range of 0.05 to 0.1 Hz are very similar between Fig. 5.a and b, especially when the comparison is done with JON-H. This is thought to be related to the most frequent location of the primary peaks, and to the fact that the spectral shape is still better captured (or more similar to the hindcast) in the neighborhood of the peaks.

Atmospheric conditions and sea states characteristics in the North Sea are indeed different from those found along coasts exposed to the

North Atlantic storm and swells like the IRE location. Therefore, it is expected to have different results at NED (Fig. 6). Here the highest levels of energy are found between 0.1 and 0.2 Hz. Once again a fix γ = 3.3 when using JON-G gives the largest differences, especially within 0.01 and 0.15 Hz, reaching NMD values close to 50% when comparing only uni-modal spectra (Fig. 6.a). It is once more verified that, with JON-H, MD values are effectively reduced, ranging between −0.05 and 0.06 m^2 s when the comparison is done with uni-modal sea states. As observed before at IRE, when hindcast spectra is compared with the time series created with JON-H, the NMD are close to 0% within the frequency range where the highest mean energy is concentrated (0.1 to 0.2 Hz in this case). Similar MD and NMD are observed when the full time series is employed (Fig. 6.b).

The SI at NED shows larger changes, at lower frequencies in the 0.05 to 0.1 Hz range, between results obtained using uni-modal sea states only and the full time series of spectra for 2021. Note that, in Fig. 6.b the SI can be >225% for frequencies <0.08 Hz using either JON-G or JON-H. At the same time there are small variations in SI levels for frequencies >0.20 Hz between Fig. 6.a and b, with an SI increase of about 5% in average when the comparison is made with the full spectra time series. This is thought to be related to the occurrence of the main spectral peaks at frequencies >0.08 Hz and secondary peaks typically occurring at lower frequencies, which is also reflected in the larger changes of NMD between Fig. 6.a and b.

These results show that, in general, mean levels of energy can be well approximated with JON-H in the frequency range where most of the energy from the sea states is concentrated, which is related to the location where the dominant peaks occur and that are better represented. It is also clear that using an inadequate fixed γ parameter (JON-G) can lead to larger over or underestimations of the spectral peaks. The SI results provide insights regarding the intrinsic differences in the wave spectrum evolution in time. Comparisons using only uni-modal sea states show the smaller values of SI in the neighborhood of the frequencies containing the largest energy, nevertheless, the minimum SI is still close to 10%. These levels notably increase towards shorter frequencies although they are related to very low mean energy levels. It is possible that part of the mean differences and SI, of the reconstructed time series of spectra compared to the hindcast data, can be mitigated employing techniques to incorporate multi-modality like the ones proposed by Guedes Soares (1984) or Ricondo et al. (2024).

4.3. Power production estimations

The analysis in Section 4.2 showed the changes on wave energy distribution, across frequencies, when different approaches are used to reconstruct the spectrum compared to the reference hindcast spectra. Here, the effects of those changes on estimations of wave power production are quantified. To this aim, the response of a point-absorber WEC (see Section 3.3) is modeled using JON-G, JON-H and FSR for the input time series. Power production estimations are done for a 30 years period. The gamma values used when JON-G is employed, are computed for each selected location (POR, IRE, NED) as specified in Section 3.4.

An example of the spectral shapes used as input for the simulation of the point absorber at POR (2 different time steps), is presented in Fig. 7. The mean γ used for JON-G was obtained using 30 years of modeled spectra. Note that even when an "adequate" γ value is employed for a given location, there can still be large differences in the energy levels at the spectral peak and neighboring frequencies. Using JON-H for uni-modal sea states allows to improve spectral representation. As a result, H_s and other wave parameters obtained from spectral integration are closer to those from the reference spectra. This is not the case for multi-modal sea states with secondary peaks which energy levels are similar to the main peak. For these scenarios, the spectral shape obtained with JON-H can neglect the presence of spectral energy in the frequency

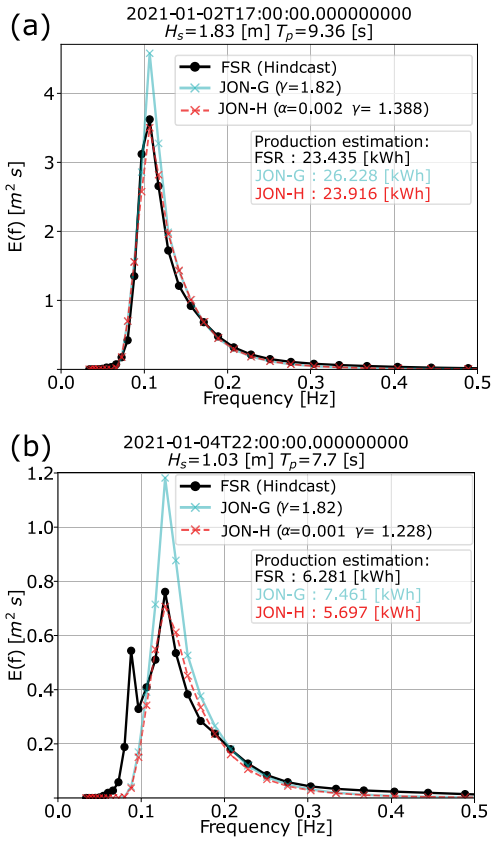

Fig. 7. Differences in the spectral energy distribution used when input for WEC simulations is done with FSR, JON-H and JON-G. Examples for (a) uni-modal and (b) bi-modal sea state at POR location.

ranges of the secondary peaks. This latter effect, directly related to the optimization method used to obtain α and γ, is observed in Fig. 7.b.

Let us now pay attention to the differences in mean power production estimations that occur as a consequence of the spectral shapes. In Fig. 7.a (uni-modal case), 23.43 kWh are obtained with FSR, as expected JON-H gives similar results (23.92 kWh) with a slight difference of ~2%, and a clear overestimation is obtained with JON-G reaching 12% compared to FSR. For the bi-modal example resented in Fig. 7.b, estimated production with FSR is 6.28 kWh. As discussed above, there is a significant portion of spectral energy not considered with JON-H, for frequencies <0.106 Hz (this is also true for JON-G). Thus, it is not surprising to obtain less power production with JON-H compared to FSR, leading to a 9.3% underestimation. Once again, the energy excess in the neighborhood of the peak, obtained with JON-G, causes a large production overestimation of about 19%.

Fig. 7 provides a comprehensive example of the spectral shapes' effect over power production, but for a robust quantification of the overall bias introduced in production assessments, a long term analysis is required. The yearly production yields estimated for 30 years (1992 to 2021) is presented in Fig. 8. On all left panels the MWh amount is included to show the production levels at each location (POR, IRE and NED), while in the NMD with respect to FSR are included on the right panels. Even though there is a clear inter annual production variability, certainly related to the wave conditions of each year, there is an almost consistent NMD level throughout the 30 years at the 3 locations (Fig. 8.a, b and c). Production overestimation levels with JON-G, are similar at POR and NED with NMD that can be ≥12.5%. Differences are only slightly smaller at IRE (Fig. 8.b) with NMD levels ranging between 11 and 12%. These are non negligible discrepancies indeed, for example, while the total 30 years power production estimated at POR using FSR

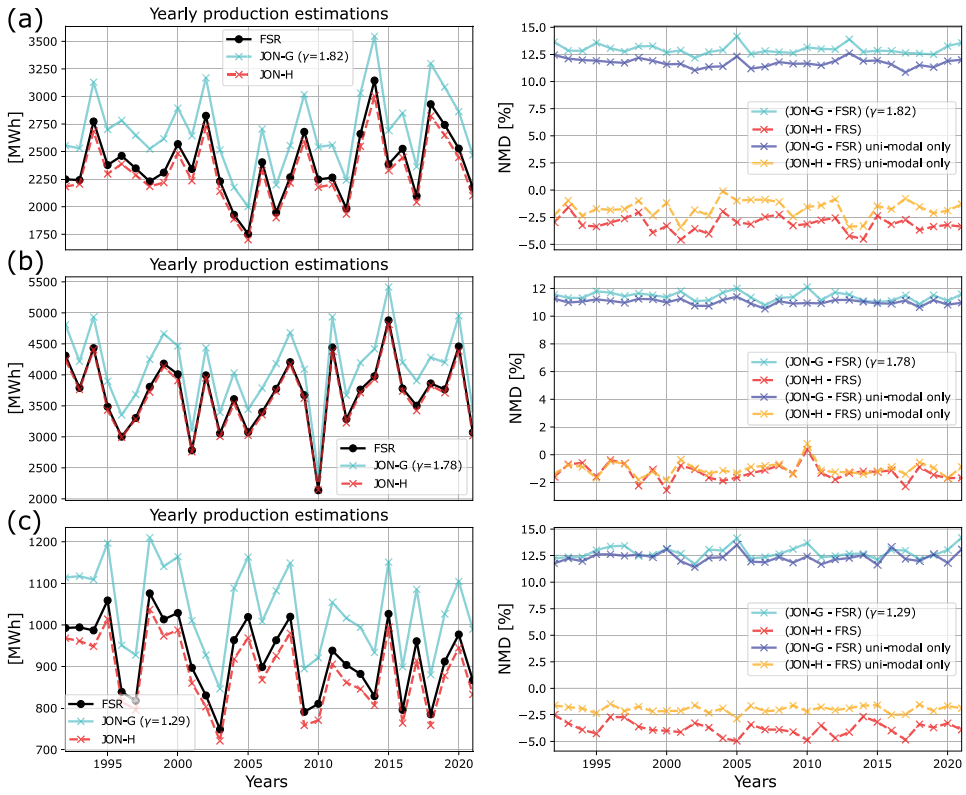

Fig. 8. Yearly power production (left) and production differences with respect to FSR (right) at (a) POR, (b) IRE, and (c) NED. Blue and orange lines in right panels correspond to NMD computed using the power production obtained from uni-modal sea states only.

is 71614.8 MWh, 80894.9 MWh are obtained with JON-G, implying a ∼12.9% overestimation. In contrast, when a more detailed spectral representation is employed with JON-H, NMD levels are considerably small, although in this case there is a tendency to underestimate power production. When JON-H is used NMD can be larger than −2.5% at POR and NED (even reaching −5%), and mostly between −1 and −2% at IRE. It should be pointed out that no capping was applied to these production estimations.

Similar to the approach taken in Section 4.2, the NMD computed using yearly production from uni-modal sea states only is included in Fig. 8 (right panel). This is done to further analyze the influence of the spectral shapes in production differences. Although small, most noticeable changes in NMD occur at POR and NED when JON-H is employed. Compared to the previous analysis using the full 30 years time series, there is a reduction of the production underestimation that ranges between 1 to 2.5% (see orange and red lines on right panel of Fig. 8.a,c). Only negligible changes are observed at IRE. It is thought that this behavior is related on first place, to the frequency of occurrence of uni-modal (and multi-modal) sea states, and secondly, to the amplitude (energy level) of the secondary peaks at each location. Note that POR and NED has similar occurrences of uni-modal (typically ≤60%) and multi-modal sea states, while at IRE a clear dominance of uni-modal sea states is observed (∼68% for the considered E(f) threshold; Table 2). The minimum changes of production NMD at IRE suggests that the energy carried at secondary peaks is considerably smaller than that of the main peaks. Thus, even if the spectral energy distribution is not perfectly represented with JON-H, the method still allows to capture the general characteristics from the spectra. This is aligned with the results from Fig. 5 (see changes in E(f) NMD).

When spectral input is done using JON-G, changes in the NMD of production, related to the use of full time series or just uni-modal sea states, are almost negligible at IRE and NED (see dark and light blue lines in right panels from Fig. 8). At POR, there is a mean NMD reduction of about 2.5%. It was verified that the coefficient of variation (CoV = std/mean) of γ (Eq. (14)) at POR, computed for the 30 years, is similar to the one estimated at IRE (CoVs of 0.44 and 0.41 respectively). On the other hand the γ CoV at NED is comparatively small (0.22). This supports the idea that there is a larger amount of spectral energy contained in the neighborhood of secondary peaks at POR, and therefore, the production overestimation is larger when the full time series is employed. At the same time, this could also confirm that the energy carried by secondary peaks at IRE is lower, and thus, minimum changes in the NMD are observed for both, JON-H and JON-G (Fig. 8.b; right panel).

Regarding the obtained results, it is expected that even with a non-linear model, the percentage differences in the power produced would be in the same range for the different spectral representation methods. However, greater differences in the absolute values are probable in the high resource regions like POR and IRE (related to the occurrence wave heights >5 m), compared to the low resource regions (NED). One should also be aware of these results' context. There are certainly other sources of uncertainties that should be studied as well, regarding WECs simulations or accuracy of wave model results for example Bitner-Gregersen et al. (2022). The latter one mainly related to the accuracy of the forcing fields, physical processes included in parameterizations and numerical choices (e.g.; Alday et al., 2021; Cavaleri and Bertotti, 1997; Ardhuin et al., 2010; Roland and Ardhuin, 2014). The obtained results are only related to how the representation of the wave spectrum can affect production estimates.

It is also important to highlight that, for a single axis-symmetric WEC like the point-absorber, the effect of directionality of waves does not have an effect on the obtained results (device response). This is why we have employed the frequencies spectrum to assess the effect of spectral shapes in production estimations. Nevertheless, wave directionality becomes an additional necessary part of the sea states description when analyzing WEC arrays. Directionality of wave energy will play an important role in the WECs' interactions, affecting power

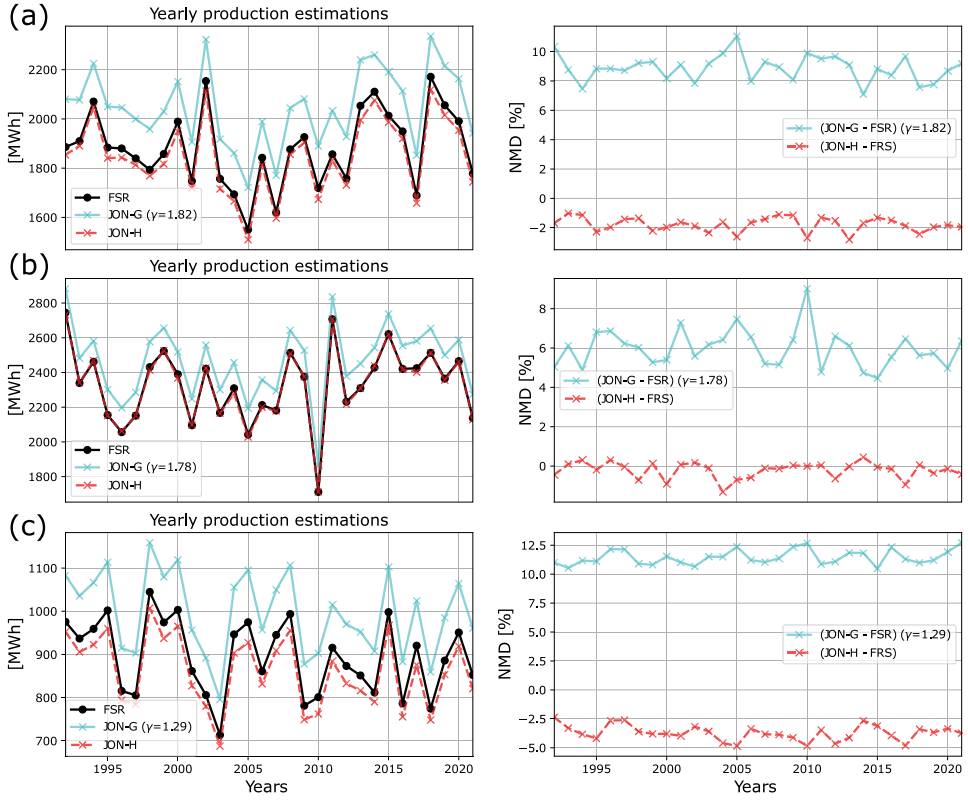

Fig. 9. Yearly power production with capping applied at 500 kW (left) and production differences with respect to FSR (right) at (a) POR, (b) IRE, and (c) NED.

production estimates. In the case of arrays' operation analysis, the directional spectrum must be incorporated.

In Appendix B, a map with mean gamma values for the European coastal shelf is included in Fig. 11. This map was created using 4768 spectral files from the ECHOWAVE hindcast. Since the JONSWAP spectrum is still commonly used, we expect that this recommended values will help to reduce errors in general practical applications. Adequate gamma values for other parts of the world can be obtained from Mazzaretto et al. (2022).

4.4. Effects of capped power in production estimations

When a limitation is set to power production of a WEC, in essence, the response of the device does not (fully) follow the spectral characteristics or spectral input anymore. These changes in the dynamic response of the device, due to the capping approach to control the power output, are very difficult to implement when considering irregular sea states in WEC models working in the frequency domain, and are not considered in the simulations employed here. In this case, the effects of power capping are included in a simplified way by setting the production to a defined maximum whenever the estimation of produced power is larger than that threshold. Power production capping is frequently implemented in operating devices and prototypes, which is why it is of interest to verify its effect on production differences (NMD).

An estimation of the yearly production obtained for 30 years with JON-G, JON-H and FSR, including a power cap at 500 kW, is presented in Fig. 9. Compared to the results obtained in Fig. 8, there is a clear reduction of the total production obtained for the 30 years window when the 500 kW capping is applied. This reduction is of course related to the local wave characteristics, and the capping will have a larger effect in those locations with higher resource (or higher mean energy flux). For example, there is a 20% reduction at POR, 36% at IRE and only 2.8% at NED (with JON-H and FSR). As mentioned above, when the power cap is applied, the response of the WEC does not completely follow the spectral input that characterizes wave conditions. In this case, this helps to reduce the production overestimation obtained with JON-G, especially in the high resource sites POR and IRE where the NMD with respect to FSR, in average, is roughly reduce by 3.5 and 5.5% (light blue lines on left panels of Fig. 9.a, b compared to Fig. 8.a, b). Thus, capping the power production can have a compensating effect that helps to partially reduce production overestimation when the JONSWAP spectrum is employed. Nevertheless, as observed in Fig. 9, this will depend on the power level where the capping is applied related to local resource conditions.

Although slightly out the main scope of this study, the effect of production capping over the capacity factor (CF) was analyzed to verify its changes related to each spectral input approach. The capacity factor is commonly expressed as the production yield over the WEC's maximum possible power production (P_{max}) times the operation period in hours ($CF = \text{Prod.}/(P_{max}\Delta t)$). In Fig. 10, the yearly CF values are estimated at POR using JON-G, JON-H, and FSR, for cases without and with power capping applied to production at 500 kW and 300 kW. For the cases without capping (as done in all previous examples), P_{max} is defined as the mean of the maximum production from each year to have a reference value representative of the 30 year time window (P_{max} = 2779.6 kW in this case). Note that when no capping is applied, regardless of the spectral shapes (JON-G, JON-H, or FSR), CF values are very similar ($\leq$0.1). This is due to the high production levels obtained when the WEC response follows the input spectra and, as a consequence, the high P_{max} used to compute CF. Differences of the CF between JON-G, compared to JON-H or FSR, arise as the capping to production is increased. In average, CF obtained when production is estimated using JON-G is 8.8% higher than the CF obtained with JON-H or FSR when capping is applied at 300 kW or 500 kW. This is also valid when a power production capping is applied at 400 kW (not shown).

It should be noticed that, although the CF levels increase as P_{max} is capped at lower values, the total production is actually reduced. For example at POR, total production estimated for 30 years (with FSR) is 71614 MW when no capping is applied. Then total production yield drops to 56422 MW when capping is applied at 500 kW. This suggests

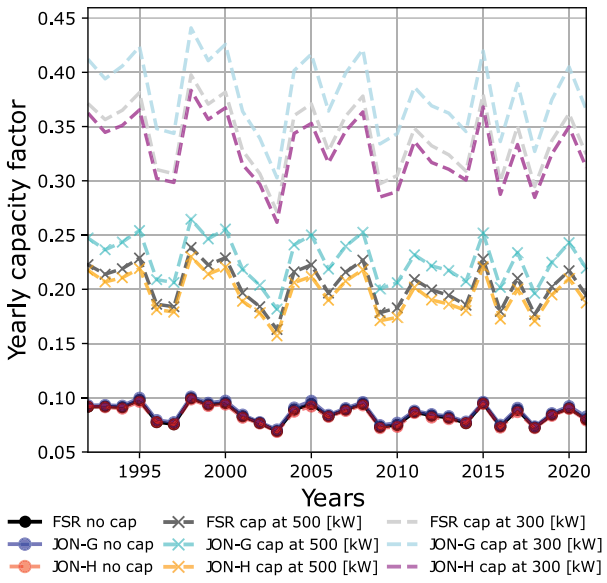

Fig. 10. Yearly capacity factors estimated without and with power capping applied to WEC's production. Analyzed location: POR.

that using purely the CF as measure of a device's power production efficiency might be misleading. Differences in production levels estimated with a time domain model, where incorporating capping effects can be better represented, might vary depending on the occurrences of wave conditions that meet the imposed operation thresholds. Nevertheless the main identified behavior still holds true: CF higher values can be influenced by users setting upper limits either due to PTO size or to nominal capacities desired. This can lead to CF being high, as the nominal capacity is achieved at "lower" conditions and maintained for longer instances, leading to a higher rate of utilization.

5. Conclusions

In the present paper we have analyzed the effects of spectral representation and the occurrences of multi-modal sea states on power production estimations from a point absorber wave energy converter. The proposed analyses were based on WEC responses obtained from weakly non-linear simulations done with HAMS-MREL model. To assess the effects of sea states characterization in terms of wave energy distribution, 3 approaches were proposed to define the input for WEC simulations. Two of them based on the use of the JONSWAP spectrum JON-G and JON-H, which do not take into account multi-modality, and one based on the use of spectral data from the ECHOWAVE hindcast (FSR). The latter is taken as reference for comparison purposes since wave models allow to successfully simulate different spectral shapes including the evolution of multi-modal spectra. To take into account different wave conditions in the analysis, 3 locations were studied: off the coasts of Portugal (POR), Ireland (IRE), and The Netherlands (NED).

Site characterization showed that, in all analyzed locations, there is a high frequency of occurrence of multi-modal sea states (in general >30%; see Table 2). There are clear differences in the spectral energy distribution related to the method used to "reconstruct" or represent the spectrum. Nevertheless, outside the frequency range where most of the energy is located (related to the position of the main peaks), differences (NMD) and SI levels of JON-G and JON-H, with respect to the hindcast spectral data, are mainly due to the parametric shape of the JONSWAP spectrum and less influenced by the occurrence of secondary peaks. Particularly for higher frequencies (>0.2 Hz up to 0.6 Hz), there is a clear reduction of the SI when spectral comparison is done using uni-modal sea states only.

When reconstructing the spectral time series using the JON-H approach, overall differences can be effectively reduced if adequate values of α and γ are employed at each given time step, reaching NMD levels close to 0% within the most energetic frequencies range. This is true when the comparison is done using the full time series of spectra or just with uni-modal sea states, which implies that with a proper modulation of the JONSWAP spectrum, as proposed by Hasselmann et al. (1973), the main characteristics of the energy distribution can be well represented. As a consequence, when WEC production is simulated using the spectra time series generated with JON-H, results are closer to the estimations done with FSR, with a tendency to underestimate up to −5% yearly power production. At POR and NED these underestimations are reduced by ~2.5% when the comparison is done considering uni-modal sea states only, which suggests that the energy carried at secondary peaks is significant.

Using traditional methods that apply the JONSWAP spectrum as done with JON-G, even with an adequate gamma value, production overestimation can be >12% (in some cases close to 15%) compared to the results obtained with the hindcast's reference spectra. When power capping is applied to the WEC production, these differences are partially reduced but they can still be >8% depending on the wave conditions of the analyzed location. Since the JONSWAP spectrum is still commonly used in wave energy applications, quantifying the differences or errors, that arise as a result of its use, becomes of high importance to properly incorporate uncertainties in production estimations. Overestimating the capabilities of sites across Europe, while at face value may be a "positive" outcome, it will most probably lead to significant increases in project risks. With expected revenues over-estimated, a lot of project may fall apart and quickly hinder the further development of the wave energy sector. This becomes even more important in economic evaluations when planning for large scale deployments, as they will require more accurate data and methods to estimate production potentials.

Extending the proposed methodology to incorporate directionality effects over WEC farms, and completing the analysis of the spectral shapes' effects over production estimations from different WEC types, are subjects of ongoing research considered for a follow-up publication. The application of the present analysis employing a time domain model for the WEC response is also considered for future research work. This would allow to compare (with BEM results), and further understand the level of uncertainties in power production estimations related to the sea states representation.

CRediT authorship contribution statement

Matías Alday: Writing – review & editing, Writing – original draft, Visualization, Validation, Methodology, Investigation, Formal analysis, Conceptualization. **Vaibhav Raghavan:** Writing – review & editing, Writing – original draft, Methodology, Investigation, Formal analysis. **George Lavidas:** Writing – review & editing, Resources, Investigation, Funding acquisition.

Declaration of competing interest

The authors declare that they have no known competing financial interests or personal relationships that could have appeared to influence the work reported in this paper.

Acknowledgments

We would like to thank Jian Tan (j.tan-2@tudelft.nl) for the fruitful discussions and insights on WEC simulations and the content of this study. Many thanks to the anonymous reviewers for their constructive input and suggestions to improve the content of this manuscript.

This work is part of the EU-SCORES project that has received funding from the European Union's Horizon 2020 research and innovation programme under grant agreement No 101036457 (https://euscores.eu)

Appendix A. Script to find JONSWAP parameters using best fit method

Below the implemented Python script to find the parameters which provide the best fit between Eq. (17) and the frequency spectra from the ECHOWAVE hindcast is provided. It should be noticed that the variable goda_first_guess was set to "True" in all JON-G computations to estimate the mean γ parameter.

```
#-------------------------------------------------------------------------#
#    FIND JONSWAP PARAMETERS BASED ON BEST FIT COMPARED TO WW3 SPECTRUM    #
#    by Matias Alday G.; creation date: May 17th 2024                      #
#-------------------------------------------------------------------------#
import numpy as np
import xarray as xr
from scipy.stats import pearsonr
from scipy.optimize import minimize

def JONSWAP_best_fit(w3_ef,Hs,f_p,freqs,goda_first_guess):
    # w3_ef : WW3 1D spectrum from xarray dataset , ex. DS.ef[1]
    # Hs    : WW3 significant wave height from xarray dataset , ex. DS.hs[1]
    # f_p   : WW3 peak frequency from xarray dataset , ex. DS.fp[1]
    # freqs : discrete frequencies from WW3 (taken from 1D spectra file)
    # goda_first_guess : set to True or False to activate/deactivate first
    #         alpha guess using Goda 1999 JONSWAP expression

    # JONSWAP spectrum expression (Hasselmann 1973)
    def E_jon(a, g, f_peak, freq):
        s=np.where(freq > f_peak, 0.09,0.07)
        r=np.exp(-((freq-f_peak)**2)/(2*(s**2)*(f_peak**2)))
        return ((a*9.8**2)/(((2*np.pi)**4)
         ↪  *(freq**5)))*np.exp((-5/4)*(f_peak/freq)**4)*g**r
    #-------------------------------------------------------------------------#

    if goda_first_guess:
        # Goda 1999 JONSWAP approximation (used for initial guess of gamma):
        def E_goda(g,H_s, f_peak, freq):
            # eq. 2.13 in Goda 1999
            Bj=(0.0624/(0.230+0.0336*g-0.185*(1.9+g)**-1))*(1.094-
             ↪  (0.01915*np.log(g)))
            s=np.where(freq > f_peak, 0.09,0.07) #sigma varable eq 2.14 in Goda
             ↪  1999

            return Bj*(H_s**2)*(f_peak**4)*(freq**-5)*\
            np.exp(-1.25*(freq*(f_peak**-1))**-4)*g**np.exp(-
             ↪  (((freq*(f_peak**-1))-1)**2)/(2*s**2))
        #
        # Defining the objective function to minimize (sum of squared
        ↪  differences)
        def objective(g, H_s, f_peak, frequencies, Ef):
            E_g= E_goda(g, H_s, f_peak, frequencies)
            return np.sum((E_g - Ef) ** 2)
        # initial guess for gamma parameter in Goda JONSWAP expresion
        goda_gamma_init=3.3
        # define bounds for gamma to avoid unrealistic values (as defined in
        ↪  Goda)
        gamma_bounds = [(1, 7)]
        # Iteration for optimization
        aux= minimize(objective,goda_gamma_init,
        ↪  args=(Hs,f_p,freqs,w3_ef),bounds=gamma_bounds)
        gamma_init=aux.x; gamma_init=gamma_init[0]
        #print('Hs: '+str(Hs)+ ' Peak freq. :'+str(f_p))
        #print('Goda gamma='+str(gamma_init))


        # Defining objective funtion to minimize and get alpha first guess
        def objective(params, frequencies, Ef):
            a = params
            E_j= E_jon(a, gamma_init, f_p, frequencies)
            return np.sum((E_j - Ef) ** 2)
        # Iteration for optimization
        aux= minimize(objective,gamma_init, args=(freqs,w3_ef))
        alpha_init=aux.x; alpha_init=alpha_init[0]
        #print('initial guess: aplha='+str(alpha_init)+' gamma='+str(gamma_init))
    else:
        gamma_init=3.3; alpha_init=0.02 # set by default
    #-------------------------------------------------------------------------#
    # Perform optimization to get JONSWAP's alpha and gamma
    # Defining bjjective function:
    def objective(params, frequencies, Ef_w3, f_peak):
        a, g = params
        E_ag = E_jon(a, g, f_peak, frequencies)
        return np.sum((E_ag - Ef_w3)**2)
    # Define bounds for alplha and gamma
    a_g_bounds=[(1e-4,1),(1,7)]
    # Final optimization

    init=[alpha_init,gamma_init]
    final_parameters=minimize(objective, init, args=(freqs, w3_ef,
    ↪  f_p),bounds=a_g_bounds)
    # best fit final parameters
    alpha, gamma =final_parameters.x
    # Pearson correlation parameter between WW3 and optimized JONSWAP
    P_corr,_= pearsonr(E_jon(alpha, gamma, f_p, freqs), w3_ef[0])
    # Pearson correlation parameter between WW3 and optimized Goda JONSWAP
    P_corr_goda,_=pearsonr(E_goda(gamma_init,Hs, f_p, freqs), w3_ef[0])

    # if goda_first_guess=True, outputted gamma_init corresponds to the gamma
    # parameter that gives the best fit for the Goda expression of JONSWAP
    return gamma_init,alpha_init,gamma,alpha,P_corr,P_corr_goda
```

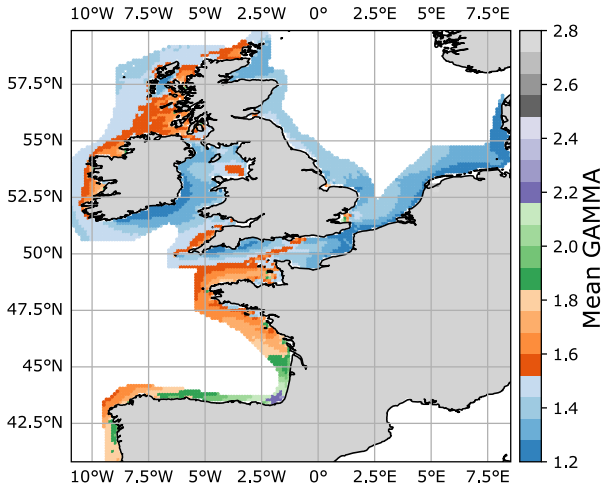

Fig. 11. Mean gamma values recommended for European coasts when using Goda's JONSWAP expression.

Table 3
Recommended mean gamma values for Goda's JONSWAP expression.

Location	Mean gamma values as function of used time window				
	5 years (2017–2021)	10 years (2012–2021)	15 years (2007–2021)	20 years (2002–2021)	30 years (1992–2021)
POR	1.84	1.81	1.84	1.83	1.82
IRE	1.77	1.77	1.78	1.78	1.78
NED	1.30	1.29	1.29	1.29	1.29

Appendix B. Mean gamma values to apply with Goda's JONSWAP formulation in North Atlantic European waters

The mean gamma values in Fig. 11, for the JONSWAP formulation proposed by Goda, were estimated with the best fit method described in Section 3.4 using 5 years of spectral data from the ECHOWAVE hindcast by Alday and Lavidas (2024), from 2017 to 2021. The time window used was restricted to 5 years due to the number of spectral files analyzed (4768). To verify the effects of longer time windows on the mean gamma values, a simple sensitivity analysis was performed for the 3 selected locations in this study (POR, IRE, and NED; see Table 3). Results in Table 3 show that the mean values estimated with 5 years of spectral data are representative of each location.

Data availability

The ECHOWAVE hindcast wave parameters' fields output can be found in the following site:

https://www.tudelft.nl/en/ceg/about-faculty/departments/hydraulic-engineering/sections/offshore-engineering/research/marine-renewable-energies-lab-mrel/datasets-models

Spectral data can be requested to M.A. (M.F.AldayGonzalez@tudelft.nl) or G.L. (g.lavidas@tudelft.nl).

References

Adibzade, M., Akbari, H., 2024. Fully spectral approach to evaluate the performance of floating wave energy converters in directional complex sea states. Ocean Eng. 306, 117999. http://dx.doi.org/10.1016/j.oceaneng.2024.117999.

Ailliot, P., Maisondieu, C., Monbet, V., 2013. Dynamical partitioning of directional ocean wave spectra. Probabilistic Eng. Mech. 33, 95–102.

Alday, M., Accensi, M., Ardhuin, F., Dodet, G., 2021. A global wave parameter database for geophysical applications. Part 3: Improved forcing and spectral resolution. Ocean. Model. 166, 101848. http://dx.doi.org/10.1016/j.ocemod.2021.101848.

Alday, M., Ardhuin, F., Dodet, G., Accensi, M., 2022. Accuracy of numerical wave model results: application to the Atlantic coasts of Europe. Ocean. Sci. 18 (6), 1665–1689. http://dx.doi.org/10.5194/os-18-1665-2022.

Alday, M., Lavidas, G., 2024. The ECHOWAVE hindcast: A 30-years high resolution database for wave energy applications in North Atlantic European waters. Renew. Energy 121391. http://dx.doi.org/10.1016/j.renene.2024.121391.

Alves, M., 2016. Chapter 2 - frequency-domain models. In: Folley, M. (Ed.), Numerical Modelling of Wave Energy Converters. Academic Press, pp. 11–30. http://dx.doi.org/10.1016/B978-0-12-803210-7.00002-5, URL: https://www.sciencedirect.com/science/article/pii/B9780128032107000025.

Ardhuin, F., Rogers, E., Babanin, A., Filipot, J.-F., Magne, R., Roland, A., van der Westhuysen, A., Queffeulou, P., Lefevre, J.-M., Aouf, L., Collard, F., 2010. Semi-empirical dissipation source functions for wind-wave models: part i, definition, calibration and validation. J. Phys. Oceanogr. 40 (9), 1917–1941. http://dx.doi.org/10.1175/2010JPO4324.1.

Ashton, I., Johanning, L., 2015. On errors in low frequency wave measurements from wave buoys. Ocean Eng. 95, 11–22. http://dx.doi.org/10.1016/j.oceaneng.2014.11.033.

Babarit, A., 2015. A database of capture width ratio of wave energy converters. Renew. Energy 80, 610–628. http://dx.doi.org/10.1016/j.renene.2015.02.049.

Benoit, M., Marcos, F., Becq, F., 1997. Development of a third generation shallow-water wave model with unstructured spatial meshing. In: Coastal Engineering 1996. pp. 465–478.

Besio, G., Mentaschi, L., Mazzino, A., 2016. Wave energy resource assessment in the mediterranean sea on the basis of a 35-year hindcast. Energy 94, 50–63.

Beyramzadeh, M., Siadatmousavi, S.M., 2022. Skill assessment of different quadruplet wave-wave interaction formulations in the WAVEWATCH-III model with application to the Gulf of Mexico. Appl. Ocean Res. 127, 103316. http://dx.doi.org/10.1016/j.apor.2022.103316.

Bitner-Gregersen, E.M., Waseda, T., Parunov, J., Yim, S., Hirdaris, S., Ma, N., Soares, C.G., 2022. Uncertainties in long-term wave modelling. Mar. Struct. 84, 103217. http://dx.doi.org/10.1016/j.marstruc.2022.103217.

Booij, N., Holthuijsen, L., Ris, R., 1996. The SWAN wave model for shallow water. In: Coastal Engineering 1996. pp. 668–676. http://dx.doi.org/10.1061/9780784402429.053.

Boukhanovsky, A., Guedes Soares, C., 2009. Modelling of multipeaked directional wave spectra. Appl. Ocean Res. 31 (2), 132–141. http://dx.doi.org/10.1016/j.apor.2009.06.001.

Bradbury, A., Mason, T., Poate, T., 2007. Implications of the spectral shape of wave conditions for engineering design and coastal hazard assessment–evidence from the english channel. In: 10th International Workshop on Wave Hindcasting and Forecasting and Coastal Hazard Symposium North Shore, Oahu, Hawaii, November. pp. 11–16, URL: https://southerncoastalgroup-scopac.org.uk/wp-content/uploads/2018/11/Bradbury_Hawaii_2007.pdf.

Carballo, R., Sánchez, M., Ramos, V., Castro, A., 2014. A tool for combined WEC-site selection throughout a coastal region: Rias Baixas, NW Spain. Appl. Energy 135, 11–19. http://dx.doi.org/10.1016/j.apenergy.2014.08.068.

Cavaleri, L., Bertotti, L., 1997. In search of the correct wind and wave fields in a minor basin. Mon. Weather Rev. 125 (8), 1964–1975. http://dx.doi.org/10.1175/1520-0493(1997)125<1964:ISOTCW>2.0.CO;2.

Chawla, A., Tolman, H.L., Gerald, V., Spindler, D., Spindler, T., Alves, J.-H.G.M., Cao, D., Hanson, J.L., Devaliere, E.-M., 2013. A multigrid wave forecasting model: A new paradigm in operational wave forecasting. Weather. Forecast. 28, 1057–1078. http://dx.doi.org/10.1175/waf-d-12-00007.1.

Clabby, D., Henry, A., Folley, M., Whittaker, T., 2012. The effect of the spectral distribution of wave energy on the performance of a bottom hinged flap type wave energy converter. In: International Conference on Offshore Mechanics and Arctic Engineering. Vol. 44946, American Society of Mechanical Engineers, pp. 331–339. http://dx.doi.org/10.1115/OMAE2012-83398.

Corpower, 2023. Corpower. URL: https://corpowerocean.com/wave-energy-technology/.

De La Torre, D., Luyo, J., Ortega, A., 2023. On the estimation of the wave energy period and a Kernel proposal for the Peru Basin. J. Mar. Sci. Eng. 11 (6), http://dx.doi.org/10.3390/jmse11061100, URL: https://www.mdpi.com/2077-1312/11/6/1100.

De Leo, F., Cremonini, G., Corrales-González, M., Besio, G., 2024. Climate analysis of wave systems for multimodal sea states in the mediterranean sea. Appl. Ocean Res. 142, 103813. http://dx.doi.org/10.1016/j.apor.2023.103813.

Donelan, M.A., Hamilton, J., Hui, W., 1985. Directional spectra of wind-generated ocean waves. Philos. Trans. R. Soc. Lond. Ser. A, Math. Phys. Sci. 315 (1534), 509–562. http://dx.doi.org/10.1098/rsta.1985.0054.

Esmaeilzadeh, S., Alam, M.-R., 2019. Shape optimization of wave energy converters for broadband directional incident waves. Ocean Eng. 174, 186–200. http://dx.doi.org/10.1016/j.oceaneng.2019.01.029.

Everett, J., Sorokin, V., Whittaker, C., Aw, K., 2024. Numerical and experimental analysis of the power output performance of a point absorber WEC for nearshore wave conditions. Ocean Eng. 309, 118381. http://dx.doi.org/10.1016/j.oceaneng.2024.118381.

Folley, M., Whittaker, T., 2010. Spectral modelling of wave energy converters. Coast. Eng. 57 (10), 892–897. http://dx.doi.org/10.1016/j.coastaleng.2010.05.007, URL: https://www.sciencedirect.com/science/article/pii/S0378383910000700.

Folley, M., Whittaker, T., 2013. Validating a spectral-domain model of an OWC using physical model data. Int. J. Mar. Energy 2, 1–11. http://dx.doi.org/10.1016/j.ijome.2013.05.003, URL: https://www.sciencedirect.com/science/article/pii/S2214166913000040.

Gerling, T.W., 1992. Partitioning sequences and arrays of directional ocean wave spectra into component wave systems. J. Atmos. Ocean. Technol. 9 (4), 444–458. http://dx.doi.org/10.1175/1520-0426(1992)009<0444:PSAAOD>2.0.CO;2.

Giassi, M., Thomas, S., Tosdevin, T., Engström, J., Hann, M., Isberg, J., Göteman, M., 2020. Capturing the experimental behaviour of a point-absorber WEC by simplified numerical models. J. Fluids Struct. 99, 103143. http://dx.doi.org/10.1016/j.jfluidstructs.2020.103143.

Girard-Ardhuin, F., Ezraty, R., 2012. Enhanced Arctic sea ice drift estimation merging radiometer and scatterometer data. IEEE Trans. Geosci. Remote Sens. 50, 2639–2648. http://dx.doi.org/10.1109/TGRS.2012.2184124.

Goda, Y., 1999. Random Seas and Design of Maritime Structures. World scientific.

Guedes Soares, C., 1984. Representation of double-peaked sea wave spectra. Ocean Eng. 11 (2), 185–207. http://dx.doi.org/10.1016/0029-8018(84)90019-2.

Guillou, N., Chapalain, G., 2018. Annual and seasonal variabilities in the performances of wave energy converters. Energy 165, 812–823. http://dx.doi.org/10.1016/j.energy.2018.10.001.

Guillou, N., Lavidas, G., Chapalain, G., 2020. Wave energy resource assessment for exploitation—a review. J. Mar. Sci. Eng. 8 (9), 705. http://dx.doi.org/10.3390/jmse8090705.

Hals, J., Bjarte-Larsson, T., Falnes, J., 2002. Optimum reactive control and control by latching of a wave-absorbing semisubmerged heaving sphere. In: International Conference on Offshore Mechanics and Arctic Engineering, 21st International Conference on Offshore Mechanics and Arctic Engineering, Volume 4, The American Society of Mechanical Engineers (ASME, pp. 415–423. http://dx.doi.org/10.1115/OMAE2002-28172, arXiv:https://asmedigitalcollection.asme.org/OMAE/proceedings-pdf/OMAE2002/36142/415/4545242/415_1.pdf.

Hanson, J.L., Jensen, R.E., 2004. Wave system diagnostics for numerical wave models. In: 8th International Workshop on Wave Hindcasting and Forecasting, Oahu, Hawaii. pp. 231–238.

Hanson, J.L., Phillips, O.M., 2001. Automated analysis of ocean surface directional wave spectra. J. Atmos. Ocean. Technol. 18 (2), 277–293. http://dx.doi.org/10.1175/1520-0426(2001)018<0277:AAOOSD>2.0.CO;2.

Hasselmann, K., Barnett, T.P., Bouws, E., Carlson, H., Cartwright, D.E., Enke, K., Ewing, J., Gienapp, A., Hasselmann, D., Kruseman, P., et al., 1973. Measurements of wind-wave growth and swell decay during the joint North Sea wave project (JONSWAP). Ergaenzungsheft Zur Dtsch. Hydrogr. Z. Reihe A URL: https://hdl.handle.net/21.11116/0000-0007-DD3C-E.

Hasselmann, S., Brüning, C., Hasselmann, K., Heimbach, P., 1996. An improved algorithm for the retrieval of ocean wave spectra from synthetic aperture radar image spectra. J. Geophys. Res.: Ocean. 101 (C7), 16615–16629.

Hasselmann, D.E., Dunckel, M., Ewing, J., 1980. Directional wave spectra observed during JONSWAP 1973. J. Phys. Oceanogr. 10 (8), 1264–1280. http://dx.doi.org/10.1175/1520-0485(1980)010<1264:DWSODJ>2.0.CO;2.

Hauser, D., Tourain, C., Hermozo, L., Alraddawi, D., Aouf, L., Chapron, B., Dalphinet, A., Delaye, L., Dalila, M., Dormy, E., et al., 2020. New observations from the SWIM radar on-board CFOSAT: Instrument validation and ocean wave measurement assessment. IEEE Trans. Geosci. Remote Sens. 59 (1), 5–26. http://dx.doi.org/10.1109/TGRS.2020.2994372.

Hegermiller, C., Antolinez, J.A., Rueda, A., Camus, P., Perez, J., Erikson, L.H., Barnard, P.L., Mendez, F.J., 2017. A multimodal wave spectrum–based approach for statistical downscaling of local wave climate. J. Phys. Oceanogr. 47 (2), 375–386. http://dx.doi.org/10.1175/JPO-D-16-0191.1.

Henry, A., Folley, M., Whittaker, T., 2018. A conceptual model of the hydrodynamics of an oscillating wave surge converter. Renew. Energy 118, 965–972. http://dx.doi.org/10.1016/j.renene.2017.10.090.

Hersbach, H., Bell, B., Berrisford, P., Hirahara, S., Horányi, A., Muñoz-Sabater, J., Nicolas, J., Peubey, C., Radu, R., Schepers, D., et al., 2020. The ERA5 global reanalysis. Q. J. R. Meteorol. Soc. 146 (730), 1999–2049. http://dx.doi.org/10.1002/qj.3803.

Hwang, P.A., Wang, D.W., Walsh, E.J., Krabill, W.B., Swift, R.N., 2000. Airborne measurements of the wavenumber spectra of ocean surface waves. part II: Directional distribution. J. Phys. Oceanogr. 30 (11), 2768–2787. http://dx.doi.org/10.1175/1520-0485(2001)031<2768:AMOTWS>2.0.CO;2.

Kamranzad, B., Etemad-Shahidi, A., Chegini, V., 2017. Developing an optimum hotspot identifier for wave energy extracting in the northern Persian Gulf. Renew. Energy 114, 59–71. http://dx.doi.org/10.1016/j.renene.2017.03.026.

Kerbiriou, M.-A., Prevosto, M., Maisondieu, C., Clément, A., Babarit, A., 2007. Influence of sea-states description on wave energy production assessment. In: Proceedings of the 7th European Wave and Tidal Energy Conference, Porto, Portugal. pp. 11–13.

Kpogo-Nuwoklo, K.A., Olagnon, M., Guédé, Z., 2014. Wave spectra partitioning and identification of wind sea and swell events. In: International Conference on Offshore Mechanics and Arctic Engineering. Vol. 45431, American Society of Mechanical Engineers, V04BT02A058. http://dx.doi.org/10.1115/OMAE2014-24689.

Kracht, P., Perez-Becker, S., Richard, J.-B., Fischer, B., 2015. Performance improvement of a point absorber wave energy converter by application of an observer-based control: Results from wave tank testing. IEEE Trans. Ind. Appl. 51 (4), 3426–3434. http://dx.doi.org/10.1109/TIA.2015.2405892.

Kudryavtsev, V., Yurovskaya, M., Chapron, B., Collard, F., Donlon, C., 2017. Sun glitter imagery of ocean surface waves. Part 1: Directional spectrum retrieval and validation. J. Geophys. Res.: Ocean. 122 (2), 1369–1383. http://dx.doi.org/10.1002/2016JC012425.

Langodan, S., Cavaleri, L., Viswanadhapalli, Y., Hoteit, I., 2015. Wind-wave source functions in opposing seas. J. Geophys. Res.: Ocean. 120 (10), 6751–6768. http://dx.doi.org/10.1002/2015JC010816.

Lavidas, G., 2020. Selection index for wave energy deployments (SIWED): A near-deterministic index for wave energy converters. Energy 196, 117131. http://dx.doi.org/10.1016/j.energy.2020.117131.

Liu, Q., Lewis, T., Zhang, Y., Sheng, W., 2015. Performance assessment of wave measurements of wave buoys. Int. J. Mar. Energy 12, 63–76. http://dx.doi.org/10.1016/j.ijome.2015.08.003.

Maisondieu, C., Boulluec, M.L., 2016. Benefits of using a spectral hindcast database for wave power extraction assessment. Int. J. Ocean. Clim. Syst. 7 (3), 83–87. http://dx.doi.org/10.1177/1759313116649967.

Mazzaretto, O.M., Menéndez, M., Lobeto, H., 2022. A global evaluation of the JONSWAP spectra suitability on coastal areas. Ocean Eng. 266, 112756. http://dx.doi.org/10.1016/j.oceaneng.2022.112756, URL: https://www.sciencedirect.com/science/article/pii/S002980182202039X.

McNatt, J., Retzler, C., 2020. The performance of the Mocean M100 wave energy converter described through numerical and physical modelling. Int. Mar. Energy J. 3, 11–19. http://dx.doi.org/10.36688/imej.3.11-19.

Mentaschi, L., Besio, G., Cassola, F., Mazzino, A., 2015. Performance evaluation of wavewatch III in the Mediterranean Sea. Ocean. Model. 90, 82–94. http://dx.doi.org/10.1016/j.ocemod.2015.04.003.

Murphy, A.H., 1988. Skill scores based on the mean square error and their relationships to the correlation coefficient. Mon. Weather Rev. 116 (12), 2417–2424. http://dx.doi.org/10.1175/1520-0493(1988)116<2417:SSBOTM>2.0.CO;2.

Murphy, A.H., Epstein, E.S., 1989. Skill scores and correlation coefficients in model verification. Mon. Weather Rev. 117 (3), 572–582.

Penalba, M., Touzón, I., Lopez-Mendia, J., Nava, V., 2017. A numerical study on the hydrodynamic impact of device slenderness and array size in wave energy farms in realistic wave climates. Ocean Eng. 142, 224–232. http://dx.doi.org/10.1016/j.oceaneng.2017.06.047, URL: https://www.sciencedirect.com/science/article/pii/S0029801817303517.

Perignon, Y., 2017. Assessing accuracy in the estimation of spectral content in wave energy resource on the French Atlantic test site SEMREV. Renew. Energy 114, 145–153. http://dx.doi.org/10.1016/j.renene.2017.02.086.

Phillips, O., 1985. Spectral and statistical properties of the equilibrium range in wind-generated gravity waves. J. Fluid Mech. 156, 505–531. http://dx.doi.org/10.1017/S0022112085002221.

Pilgrim, M., Willison, S., 2009. Dive Into Python 3, vol. 2, Springer.

Portilla-Yandún, J., 2018. The global signature of ocean wave spectra. Geophys. Res. Lett. 45 (1), 267–276. http://dx.doi.org/10.1002/2017GL076431.

Portilla-Yandún, J., Barbariol, F., Benetazzo, A., Cavaleri, L., 2019. On the statistical analysis of ocean wave directional spectra. Ocean Eng. 189, 106361. http://dx.doi.org/10.1016/j.oceaneng.2019.106361.

Prendergast, J., Li, M., Sheng, W., 2018. A study on the effects of wave spectra on wave energy conversions. IEEE J. Ocean. Eng. 45 (1), 271–283. http://dx.doi.org/10.1109/JOE.2018.2869636.

Raghavan, V., Loukogeorgaki, E., Mantadakis, N., Metrikine, A.V., Lavidas, G., 2024. HAMS-MREL, a new open source multiple body solver for marine renewable energies: Model description, application and validation. Renew. Energy 237, 121577. http://dx.doi.org/10.1016/j.renene.2024.121577, URL: https://www.sciencedirect.com/science/article/pii/S0960148124016458.

Rascle, N., Ardhuin, F., 2013. A global wave parameter database for geophysical applications. Part 2: model validation with improved source term parameterization. Ocean. Model. 70, 174–188. http://dx.doi.org/10.1016/j.ocemod.2012.12.001.

Rhinefrank, K., Schacher, A., Prudell, J., Hammagren, E., von Jouanne, A., Brekken, T., 2015. Scaled development of a novel wave energy converter through wave tank to utility-scale laboratory testing. In: 2015 IEEE Power & Energy Society General Meeting. IEEE, pp. 1–5. http://dx.doi.org/10.1109/PESGM.2015.7286008.

Ribeiro, P., Henriques, J., Campuzano, F., Gato, L., Falcão, A., 2020. A new directional wave spectra characterization for offshore renewable energy applications. Energy 213, 118828. http://dx.doi.org/10.1016/j.energy.2020.118828.

Ricondo, A., Cagigal, L., Pérez-Díaz, B., Méndez, F.J., 2024. Introducing bimodal sea-states in a hybrid model for nearshore wave processes. Coast. Eng. 192, 104556. http://dx.doi.org/10.1016/j.coastaleng.2024.104556.

Rodrıguez, G., Guedes Soares, C., 1999. A criterion for the automatic identification of multimodal sea wave spectra. Appl. Ocean Res. 21 (6), 329–333. http://dx.doi.org/10.1016/S0141-1187(99)00007-3.

Roland, A., Ardhuin, F., 2014. On the developments of spectral wave models: numerics and parameterizations for the coastal ocean. Ocean. Dyn. 64 (6), 833–846. http://dx.doi.org/10.1007/s10236-014-0711-z.

Rueda-Bayona, J.G., Guzmán, A., Silva, R., 2020. Genetic algorithms to determine JONSWAP spectra parameters. Ocean. Dyn. 70 (4), 561–571. http://dx.doi.org/10.1007/s10236-019-01341-8.

Semedo, A., Sušelj, K., Rutgersson, A., Sterl, A., 2011. A global view on the wind sea and swell climate and variability from ERA-40. J. Clim. 24 (5), 1461–1479. http://dx.doi.org/10.1175/2010JCLI3718.1.

Shao, X., Ringsberg, J.W., Yao, H.-D., Gowda, U.R.S.L., Khedkar, H.N., Todalshaug, J.H., 2024. Hydrodynamic interactions and enhanced energy harnessing amongst many WEC units in large-size wave parks. J. Mar. Sci. Eng. 12 (5), http://dx.doi.org/10.3390/jmse12050730, URL: https://www.mdpi.com/2077-1312/12/5/730.

Silva, L., Sergiienko, N., Pesce, C., Ding, B., Cazzolato, B., Morishita, H., 2020. Stochastic analysis of nonlinear wave energy converters via statistical linearization. Appl. Ocean Res. 95, 102023. http://dx.doi.org/10.1016/j.apor.2019.102023, URL: https://www.sciencedirect.com/science/article/pii/S0141118719307230.

Strong, B., Brumley, B., Terray, E., Stone, G.W., 2000. The performance of ADCP-derived directional wave spectra and comparison with other independent measurements. In: OCEANS 2000 MTS/IEEE Conference and Exhibition. Conference Proceedings (Cat. No. 00CH37158). Vol. 2, IEEE, pp. 1195–1203. http://dx.doi.org/10.1109/OCEANS.2000.881763.

Tan, J., Tao, W., Laguna, A.J., Polinder, H., Xing, Y., Miedema, S., 2023. A spectral-domain wave-to-wire model of wave energy converters. Appl. Ocean Res. 138, 103650. http://dx.doi.org/10.1016/j.apor.2023.103650, URL: https://www.sciencedirect.com/science/article/pii/S0141118723001918.

The WAVEWATCH III® Development Group, 2019. User Manual and System Documentation of WAVEWATCH III ® Version 6.07. Tech. Note 333, NOAA/NWS/NCEP/MMAB, College Park, MD, USA, 465 pp. + Appendices.

Tolman, H.L., 2008. A mosaic approach to wind wave modeling. Ocean. Model. 25, 35–47. http://dx.doi.org/10.1016/j.ocemod.2008.06.005.

Tracy, B., Devaliere, E., Hanson, J., Nicolini, T., Tolman, H., 2007. Wind sea and swell delineation for numerical wave modeling. In: 10th International Workshop on Wave Hindcasting and Forecasting & Coastal Hazards Symposium, JCOMM Tech. Rep. Vol. 41, p. 1442, URL: http://www.waveworkshop.org/10thWaves/Papers/10th_wave_paper_tracy_dhnt.pdf.

Van Rossum, G., Drake, F.L., 2009. Python 3 Reference Manual. CreateSpace, Scotts Valley, CA.

Vettor, R., Soares, C.G., 2020. A global view on bimodal wave spectra and crossing seas from ERA-interim. Ocean Eng. 210, 107439. http://dx.doi.org/10.1016/j.oceaneng.2020.107439.

Vincent, L., Soille, P., 1991. Watersheds in digital spaces: an efficient algorithm based on immersion simulations. IEEE Trans. Pattern Anal. Mach. Intell. 13 (06), 583–598, URL: https://cse.msu.edu/~cse902/S03/watershed.pdf.

Virtanen, P., Gommers, R., Oliphant, T.E., Haberland, M., Reddy, T., Cournapeau, D., Burovski, E., Peterson, P., Weckesser, W., Bright, J., van der Walt, S.J., Brett, M., Wilson, J., Millman, K.J., Mayorov, N., Nelson, A.R.J., Jones, E., Kern, R., Larson, E., Carey, C.J., Polat, İ., Feng, Y., Moore, E.W., VanderPlas, J., Laxalde, D., Perktold, J., Cimrman, R., Henriksen, I., Quintero, E.A., Harris, C.R., Archibald, A.M., Ribeiro, A.H., Pedregosa, F., van Mulbregt, P., SciPy 1.0 Contributors, 2020. SciPy 1.0: Fundamental algorithms for scientific computing in python. Nature Methods 17, 261–272. http://dx.doi.org/10.1038/s41592-019-0686-2.

WAMDI Group, 1988. The WAM model - a third generation ocean wave prediction model. J. Phys. Oceanogr. 18, 1775–1810, URL: http://journals.ametsoc.org/doi/pdf/10.1175/1520-0485%281988%29018%3C1775%3ATWMTGO%3E2.0.CO%3B2.

Wang, D.W., Hwang, P.A., 2001. An operational method for separating wind sea and swell from ocean wave spectra. J. Atmos. Ocean. Technol. 18 (12), 2052–2062. http://dx.doi.org/10.1175/1520-0426(2001)018<2052:AOMFSW>2.0.CO;2.

Wyatt, L.R., Green, J.J., Middleditch, A., 2011. HF radar data quality requirements for wave measurement. Coast. Eng. 58 (4), 327–336. http://dx.doi.org/10.1016/j.coastaleng.2010.11.005.

Young, I., 1994. On the measurement of directional wave spectra. Appl. Ocean Res. 16 (5), 283–294. http://dx.doi.org/10.1016/0141-1187(94)90017-5.